Numerical treatment of a discontinuous top surface in 2D shallow water mixed flow modeling

Numerical treatment of a discontinuous top surface in 2D shallow water mixed flow modeling

A. Maranzoni*,† and P. Mignosa

Department of Engineering and Architecture, University of Parma, Parco Area delle Scienze 181/A, 43124 Parma, Italy

*Correspondence to: Andrea Maranzoni, Department of Engineering and Architecture, University of Parma, Parco Area delle Scienze 181/A, 43124 Parma, Italy.

†E-mail: andrea.maranzoni@unipr.it

SUMMARY

This paper presents a numerical strategy based on shallow water equations (SWE) coupled with the 2D Preissmann slot model to handle a ceiling step discontinuity in finite volume schemes for mixed flow modeling. In practice a typical situation would be a closed structure, such as a bridge or culvert, which induces a sudden vertical flow constriction and may even run partly or totally full in high flow conditions. In such case, both the inlet and outlet of the structure involve a discontinuity in the top elevation. This special singularity is topologically represented by inserting a fictitious cell between two adjacent computational cells characterized by sharply different ceiling elevation. The 2D SWE are solved by means of a well-balanced quasi-conservative Godunov-type numerical scheme based on the Slope Limiter Centered (SLIC) scheme. The flow variables at each boundary of the fictitious cell are reconstructed by adopting the cross-sectional shape of the adjoining cell. Accordingly, the dynamic effect of the structure deck on the flow is suitably modeled and the *C*-property for a stationary solution is rigorously satisfied, even when the closed structure is partially full. The capability of the numerical scheme is verified by comparison with both novel analytical solutions of 1D Riemann problems with a ceiling step discontinuity and experimental data of steady and unsteady mixed flows available in literature. Finally, a real-scale application to a multiple arch bridge is presented. The results show that the method is robust and effective in predicting the 2D features induced by a crossing structure on the flow dynamics.

KEY WORDS**:** mixed flow; Preissmann slot model; ceiling step discontinuity; 2D shallow water equations; well-balanced scheme; bridges and culverts

1. INTRODUCTION

Two-dimensional (2D) modeling of unsteady free surface flows based on the shallow water approximation is widely used in practice to predict flood dynamics (e.g. [1–4]) and to assess the hydraulic hazard in flood-prone areas (e.g. [3, 5, 6]). However, in many practical applications, the presence of crossing structures which may interfere with the flow must be taken into account. Indeed, bridges and culverts may obstruct the flow significantly, thus inducing a backwater effect upstream (e.g. [7–10]) with consequent potential increase of flood hazard in the surrounding areas. Furthermore, road infrastructures (such as viaducts, underpasses, tunnels, etc.) can significantly affect the flood propagation. During severe events, such structures may run partly or totally full, with the ceiling under pressure over a portion or even over the full extent of the structure. Mixed flows occur in these cases, characterized by transitions between free-surface and pressurized flow regimes. The local effects induced by these structures on the flow field must be suitably taken into account so as to correctly predict the flow characteristics and, possibly, the hydrodynamic thrust exerted by the flow (e.g. [11, 12]) for structural damage assessment [13].

The near flow field is generally very complex due to the lateral and vertical contractions induced by this kind of singularities, and typically shows a marked three-dimensional (3D) character, particularly when overtopping occurs [10, 14]. Accordingly, vertical accelerations are not negligible, hence the shallow water assumption of gradually varied flow should not be considered valid locally. To overcome this difficulty in 2D shallow water modeling, numerical strategies commonly adopted consist in a synthetic representation of the effect of the structure through the introduction of suitable internal boundary conditions [15–17] or additional head losses [18]. The former method requires that special systems of equations, whose formulation depends on the specific flow condition (subcritical or supercritical, submerged or unsubmerged), are imposed and solved at both the upstream and downstream ends of the structure, whereas the latter requires that a suitable empirical formula is used to evaluate the local head losses expected. In any case, both methods can at the most only reproduce the global effect of the structure on the flow. The 2D extension of the classic Preissmann slot concept recently proposed by Maranzoni et al. [19] to model mixed flows under closed structures is a valid alternative to remove these limitations.

Due to its simplicity, the Preissmann slot model is widely used in one-dimensional (1D) mixed flow modeling in both literature (e.g. [20–22]) and commercial software packages (e.g. [23, 24]). It is based on the original idea of adding a fictitious narrow vertical slot, extending indefinitely upwards, over the crown of the conduit [25]. Pressurized flows can thus be simulated by using the free surface equations, assuming that the climb height of the liquid in the slot represents the surcharge pressure head. The slot width needs to be narrow enough to adequately reproduce the celerity of pressure waves. According to Maranzoni et al. [19], the Preissmann slot artifice can be extended to 2D mixed flows in a Cartesian domain by adding two narrow vertical slots, parallel to the two plane Cartesian directions, over the top

surface of the closed structure. This schematization leads to a modified form of the 2D shallow water equations (SWE) which can also be used to simulate pressurized flow conditions. A first significant advantage of this method is that the geometry of a closed structure, and in particular its low deck chord, can be accurately discretized based on the mesh resolution adopted. Thus, the 2D planar features of the flow field near the structure can be reasonably reproduced by applying the same governing equations and numerical solver to the whole domain, without having to introduce any local modification to the computational procedure.

However, applying the method in the presence of a ceiling step discontinuity remains a challenging task. A typical case encountered in practice concerns the inlet and outlet of crossing structures located in flooding areas. The original method by Maranzoni et al. [19] is not actually completely effective in handling this type of singularities since the dynamic action of the structure deck on the flow is neglected. This paper aims to address this issue by proposing a numerical strategy inspired by the *C*-property satisfying scheme suggested by Zhou et al. [26] to deal with a bottom step discontinuity in the context of MUSCL-Hancock SGM methods [27]. The basic idea is to insert a fictitious cell between two adjacent computational elements facing a discontinuity in the top elevation. Accordingly, the two neighboring actual cells are no longer mutually joined by the same intercell boundary, which appears to be split into two. The boundary extrapolated variables are reconstructed separately at each of the two split cell interfaces by adopting the cross-sectional shape of the directly adjoining computational cell. The governing equations are solved by using an explicit, finite volume, Godunov-type numerical scheme based on the Slope Limiter Centered (SLIC) scheme [28, 29] and expressed in quasi-conservative form [30] so that it is well-balanced, i.e. capable of correctly reproducing flow equilibria [31, 32], at a ceiling step discontinuity. For this purpose, the numerical scheme is made locally non-conservative by imposing the condition that the numerical fluxes of the momentum equation at the opposite sides of the fictitious cell differ by a hydrostatic term accounting for the pressure force exerted by the structure deck. The assumption of hydrostatic pressure distribution on the step discontinuity is consistent with the shallow water approximation and is widely adopted in the literature on well-balanced schemes for the solution of the SWE with discontinuous topography [33−36].

Continuous energy losses are assessed through the classic Manning formula. In order to include the resistance effects of top surfaces and vertical walls (lateral sides, piers, abutments, etc.) in the bottom friction term, an equivalent Manning coefficient is calculated for the bed by applying the classic Horton-Einstein methodology [37] to each computational cell, thereby also taking into account the case in which the roughness is distinctly different from the various solid boundaries.

The model is first validated by comparison with ad-hoc analytical solutions of 1D Riemann problems with a ceiling step discontinuity. For this purpose, the procedure used by Alcrudo and Benkhaldoun [38] to solve a Riemann problem with a bottom step is used here in the presence of a ceiling step. A set of 1D exact Riemann solutions is derived as a

superimposition of two moving waves (associated with the two characteristic families of the shallow water equations) joined by an intermediate steady state connection characterized by a steady discontinuity of the flow variables at the ceiling step.

Numerical results are also compared with some experimental data available in literature concerning steady and unsteady laboratory tests. It must be noted that, although wide and comprehensive experimental investigations have been carried out in literature on flows through bridges or culverts for 1D modeling purposes (e.g. [10, 39]), only a few empirical studies have focused on 2D effects of this type of flows [18, 40, 41].

Finally, the transit of a sudden flood wave under a multiple arch bridge is simulated in order to assess the model's suitability in dealing with field-scale cases.

The paper is structured as follows. The mathematical model is described in Section 2, together with the numerical method proposed for handling a ceiling step discontinuity. The validation of the model is performed in Section 3, while a real-scale application is presented in Section 4. Finally, some conclusions are drawn in Section 5.

2. MATHEMATICAL MODEL

The 2D extension of the classic Preissmann slot concept on a Cartesian grid is based on the idea that a top surface is defined for each computational cell, and two narrow vertical slots, parallel to the two plane Cartesian directions x and y, are added above (Figure 1), thereby creating an ideal lattice of orthogonal slots over all the computational domain [19]. For the single Cartesian element sketched in Figure 1, h and H denote the piezometric head and the ceiling elevation above the bottom, respectively, Δx and Δy are the cell sizes, while T_y and T_x are the widths of the slots along the x- and y-axis directions, respectively.

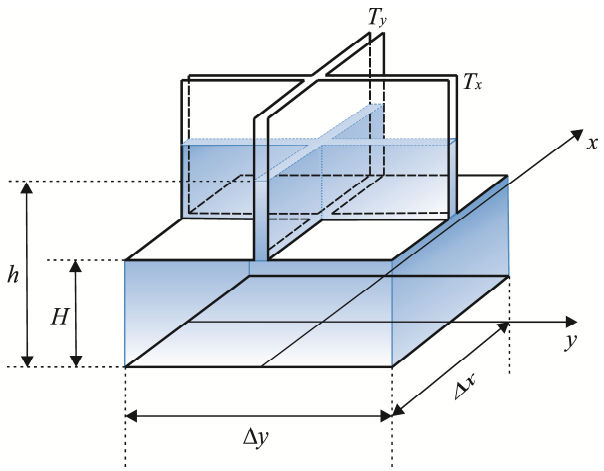

Figure 1. Definition sketch of a 2D computational element with two orthogonal slots added on the top.

2.1. Modified 2D Shallow Water Equations

The mass and linear momentum principles applied to a fixed control volume for incompressible flow under the shallow water approximation lead to the following well-known conservation form of the 2D governing equations [e.g. 28]:

$$\frac{\partial \mathbf{U}}{\partial t}+\frac{\partial \mathbf{F}}{\partial x}+\frac{\partial \mathbf{G}}{\partial y}=\mathbf{S}\,, \tag{1}$$

where **U** is the vector of the conserved variables, **F** and **G** are the flux vectors along the *x* and *y* directions, respectively, and **S** is the source term. For the Cartesian control element in Figure 1, these vectors read [19]:

$$\mathbf{U}=\begin{bmatrix}\overline{h}\\ \overline{q}_x\\ \overline{q}_y\end{bmatrix},\quad \mathbf{F}=\begin{bmatrix}\overline{q}_x\\ \overline{q}_x^2/\overline{h}_x+g\zeta_x\overline{h}_x\\ \overline{q}_x\overline{q}_y/\overline{h}_y\end{bmatrix},\quad \mathbf{G}=\begin{bmatrix}\overline{q}_y\\ \overline{q}_x\overline{q}_y/\overline{h}_x\\ \overline{q}_y^2/\overline{h}_y+g\zeta_y\overline{h}_y\end{bmatrix},\quad \mathbf{S}=\begin{bmatrix}0\\ g\overline{h}_x(S_{0x}-S_{\mathrm{fx}})\\ g\overline{h}_y(S_{0y}-S_{\mathrm{fy}})\end{bmatrix}, \tag{2}$$

where $\overline{h}$ is the average water depth over the planar area $\Delta x \cdot \Delta y$, $\overline{q}_x$ and $\overline{q}_y$ are equivalent flow discharges per unit width along the *x*- and *y*-axis directions, $\overline{h}_x$ and $\overline{h}_y$ are surface-averaged water depths over the *x*- and *y*-normal lateral faces of the control volume, while ζ_x and ζ_y are the corresponding vertical distances of the centroids from the water surface; S_{0x} and S_{0y} are the bottom slopes in the *x* and *y* directions, respectively, and S_{fx} and S_{fy} are the friction slopes along the same plane directions; finally, *g* is the acceleration due to gravity, and *t* is the time variable.

Maranzoni et al. [19] have shown that Equations (1) - (2) are strictly hyperbolic for $h > 0$ and reduce to the classic 2D SWE for free surface flows when $0 \le h \le H$.

2.2. Numerical scheme

In the present work, the homogeneous part of Equation (1) is solved by using the explicit, finite volume, second-order accurate Slope Limiter Centered (SLIC) scheme based on the First-Order Centered (FORCE) flux [28], and the source term is treated according to the second-order accurate Strang splitting decomposition [42]. Hence, the numerical scheme reads [29]:

$$\begin{aligned}
\mathbf{U}_{i,j}^{*} &= \mathbf{U}_{i,j}^{n}+\frac{\Delta t}{2}\mathbf{S}_{i,j}^{n}\\
\mathbf{U}_{i,j}^{**} &= \mathbf{U}_{i,j}^{*}-\frac{\Delta t}{\Delta x}\left[\mathbf{F}_{i+1/2,j}-\mathbf{F}_{i-1/2,j}\right]-\frac{\Delta t}{\Delta y}\left[\mathbf{G}_{i,j+1/2}-\mathbf{G}_{i,j-1/2}\right]\\
\mathbf{U}_{i,j}^{n+1} &= \mathbf{U}_{i,j}^{**}+\frac{\Delta t}{2}\mathbf{S}_{i,j}^{**}\,.
\end{aligned} \tag{3}$$

where $\mathbf{U}_{i,j}^{*}$ and $\mathbf{U}_{i,j}^{**}$ are two successive intermediate updates of the cell-average vector $\mathbf{U}_{i,j}$ at the *i*,*j*-cell in the advancing of the numerical solution from the current state $\mathbf{U}_{i,j}^{n}$ (at the time level *n*) to the update state $\mathbf{U}_{i,j}^{n+1}$ (at the time level *n*+1) in the computational time step $\Delta t = t^{n+1} - t^{n}$; $\mathbf{F}_{i\pm1/2,j}$ and $\mathbf{G}_{i,j\pm1/2}$ are the numerical fluxes in the *x* and *y* directions, respectively (computed on the basis of the cell averages $\mathbf{U}^{*}$); $\mathbf{S}_{i,j}$ is the cell-averaged source term vector.

The flow variables at cell boundaries are reconstructed by means of the MUSCL-Hancock method by applying the Van Leer slope limiter function [28, 43]. For more detail about the numerical algorithm, see Maranzoni et al. [19], and Aureli et al. [29].

Due to the explicit character of the numerical scheme, the computational time step is restricted by a Courant stability condition conveniently adapted to 2D problems [42, 19]. It should be noted that this necessary restriction significantly reduces the model efficiency when pressurization occurs, even though the pressurized flow state takes place in a very small portion of the overall computational domain [44].

The robustness and effectiveness of the numerical method were extensively tested in Maranzoni et al. [19] by comparison with both exact solutions of 1D discontinuous initial value problems and reference radial solutions of idealized test cases with cylindrical symmetry (such as the circular dam-break and the shock-focusing problem modified by introducing a uniform ceiling in the domain).

2.3. Treatment of a ceiling step discontinuity

The ceiling surface may be locally discontinuous in many practical situations involving flows through closed structures. This occurs, for example, at the inlet and outlet of a culvert or bridge, where the ceiling elevation changes abruptly from an undefined value outside the structure to a limited value inside. In this case, when the entrance and/or exit of the structure are submerged, the deck exerts a dynamic action on the flow, which must be suitably included in the momentum equation in order to correctly predict the backwater effect and the main 2D features of the flow field near the structure. For the sake of simplicity, let us consider a 1D flow in the x-direction and apply the momentum principle to the control volume enclosed between sections 1 and 2 in Figure 2, including the ceiling step discontinuity. If the dynamic thrust of the structure deck is neglected (along with the friction effects), and consequently flow states 1 and 2 are assumed to be characterized by the same specific force F, the piezometric heads h_1 and h_2 may differ significantly, since the specific force curves of the two different cross-sections are significantly different for $h > H$.

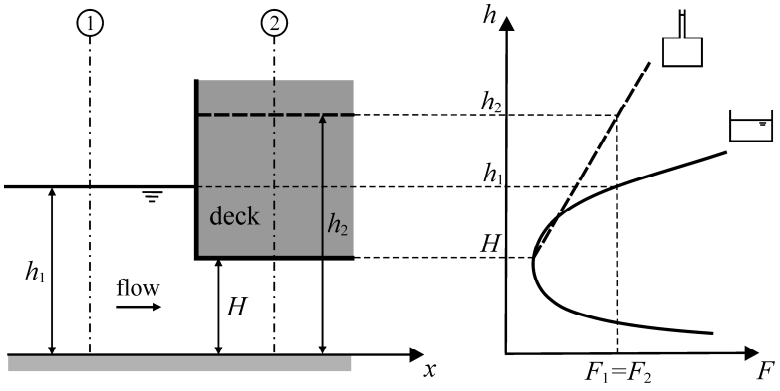

Figure 2. Analysis of the effect of a ceiling step discontinuity based on the constant specific force assumption.

In order to overcome this problem and avoid unphysical numerical predictions, the numerical technique by Zhou et al. [26], which was originally proposed to handle vertical bottom steps in free surface shallow water flows, is here adapted to the case of a ceiling step discontinuity. This technique is based on the idea of inserting a fictitious cell between two adjoining actual computational cells facing a ceiling step discontinuity (cells (i, j) and $(i+1, j)$ in the sketch in Figure 3). Hence, the intermediate cell interface $(i+1/2, j)$ is split into two distinct interfaces, $(i+1/2, j)^-$ and $(i+1/2, j)^+$, which can be treated as belonging to the (i, j)- and $(i+1, j)$-cells, respectively. The possibility of evaluating two different numerical fluxes at the two interfaces $(i+1/2, j)^-$ and $(i+1/2, j)^+$ enables to introduce the dynamic effect of the structure at a ceiling step discontinuity. Accordingly, the second step of Eq. (3) assumes the quasi-conservative form [30, 33, 35, 36, 45]:

$$\mathbf{U}_{i,j}^{**} = \mathbf{U}_{i,j}^{*} - \frac{\Delta t}{\Delta x}\left[\mathbf{F}_{i+1/2,j}^{-} - \mathbf{F}_{i-1/2,j}^{+}\right] - \frac{\Delta t}{\Delta y}\left[\mathbf{G}_{i,j+1/2}^{-} - \mathbf{G}_{i,j-1/2}^{+}\right], \tag{4}$$

in which the numerical fluxes across the – or + intercells are correspondingly labeled with a – or + superscript. Thus, with reference to the $(i+1/2, j)$-intercell, the numerical flux $\mathbf{F}_{i+1/2,j}^{-}$ is used for updating the flow variable vector $\mathbf{U}_{i,j}$ at the (i, j)-cell, whereas the numerical flux $\mathbf{F}_{i+1/2,j}^{+}$ is used for updating the cell-averaged state $\mathbf{U}_{i+1,j}$ at the $(i+1, j)$-cell. The application of the mass conservation principle to the fictitious cell in Figure 3 (acting like a very short control volume unable to store mass) leads to:

$$\left[\mathbf{F}_{i+1/2,j}^{-}\right]_1 = \left[\mathbf{F}_{i+1/2,j}^{+}\right]_1, \tag{5}$$

where the subscript reported outside the square brackets refers to the corresponding component of the flux vector. As for the momentum balance, the force exerted by the structure on the flow is assumed to be hydrostatic [36, 45], consistently with the shallow water approximation. For the case of a negative ceiling discontinuity ($H_{i+1,j} < H_{i,j}$) at the split $(i+1/2, j)^-$ and $(i+1/2, j)^+$ interfaces (Figure 3), this pressure term can be taken into account in the x-momentum equation by imposing that

$$\left[\mathbf{F}_{i+1/2,j}^{-}\right]_2 - \left[\mathbf{F}_{i+1/2,j}^{+}\right]_2 = \frac{1}{2} g \left(h_{i+1/2,j} - H_{i+1,j}\right)^2 \left(1 - \frac{T_y}{\Delta y}\right), \tag{6}$$

where $h_{i+1/2,j}$ (which satisfies the condition: $H_{i+1,\,j} \le h_{i+1/2,\,j} \le H_{i,\,j}$) is a suitable estimate at each time level of the piezometric head in the fictitious cell, computed on the basis of the water surface elevations at the neighboring cells on the left. On the other hand, in the case of a negative step completely submerged by the flow ($H_{i+1,\,j} \le H_{i,\,j} \le h_{i+1/2,\,j}$), Equation (5) is replaced by the following:

$$\left[\mathbf{F}_{i+1/2,j}^{-}\right]_2 - \left[\mathbf{F}_{i+1/2,j}^{+}\right]_2 = g\left(h_{i+1/2,j} - \frac{1}{2}H_{i,j} - \frac{1}{2}H_{i+1,j}\right)\left(H_{i,j} - H_{i+1,j}\right)\left(1 - \frac{T_y}{\Delta y}\right). \tag{7}$$

Finally, when the ceiling step does not disturb the flow (which passes under the singularity in free surface condition), it is obviously:

$$\left[\mathbf{F}^{-}_{i+1/2,j}\right]_2 = \left[\mathbf{F}^{+}_{i+1/2,j}\right]_2 . \tag{8}$$

The additional pressure force potentially due to the step singularity at the (i+1/2, j)-interface does not affect the y-momentum balance, thus:

$$\left[\mathbf{F}^{-}_{i+1/2,j}\right]_3 = \left[\mathbf{F}^{+}_{i+1/2,j}\right]_3 . \tag{9}$$

Similar relations can be derived for a positive ceiling step discontinuity ($H_{i+1,j} > H_{i,j}$) and in the y-direction. As a consequence of Equations (6) and (7), the numerical scheme may be only locally non-conservative at ceiling step discontinuities. The numerical expedient of inserting a fictitious cell can automatically be extended to each cell interface, including the ones at which the ceiling elevation is not discontinuous. In this case, the fictitious cell is actually ineffective and the numerical fluxes at the split boundaries (i+1/2, j)$^-$ and (i+1/2, j)$^+$ are exactly equal ($\mathbf{F}^{-}_{i+1/2,j} = \mathbf{F}^{+}_{i+1/2,j}$), thereby satisfying the telescopic property of the numerical fluxes typical of the conservative schemes.

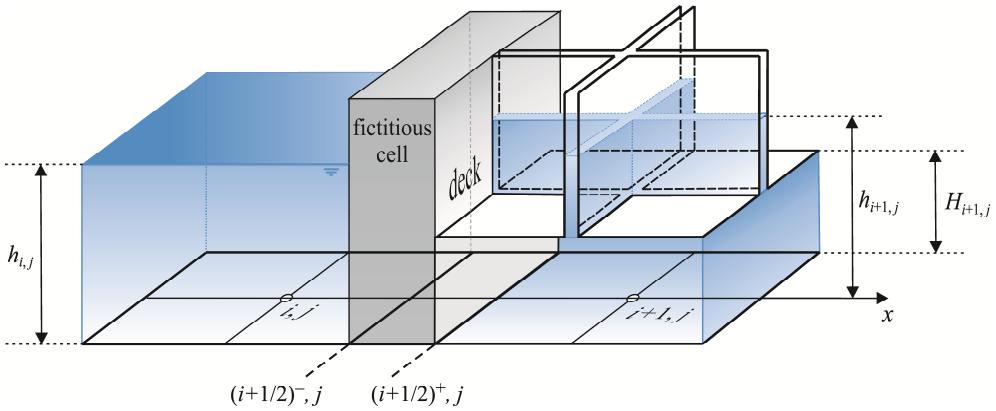

Figure 3. Representation of a ceiling step discontinuity in the 2D finite volume discretization by inserting a fictitious cell.

The evaluation of the numerical fluxes at cell interfaces requires the estimate of the conserved flow variables on the left- and right-hand sides of each intercell boundary. In this paper, the boundary extrapolated variables are assessed through the classic linear one-sided MUSCL-Hancock reconstruction [28, 42] (Figure 4). According to the SGM technique, the extrapolation of the piezometric head $\eta = h + z$ above a horizontal reference plane (being z the bottom elevation above this plane) is more advisable than the extrapolation of h in order to guarantee exactly the C-property for a stationary solution on non-flat topography [27]. In the x-direction, for the left- (L) and right-hand (R) side of the split interfaces (i+1/2, j)$^-$ and (i+1/2, j)$^+$ located at a vertical ceiling step (the j-index is dropped in Figure 4 for the sake of simplicity), it reads:

$$h^{\mathrm{L}}_{(i+1/2)^-,j} = \eta^n_{i,j} + \frac{1}{2}\Phi\left(\eta^n_{i,j} - \eta^n_{i-1,j}\right) - z_{i,j}\,, \qquad h^{\mathrm{L}}_{(i+1/2)^+,j} = \eta^n_{i,j} + \frac{1}{2}\Phi\left(\eta^n_{i,j} - \eta^n_{i-1,j}\right) - z_{i+1,j}\,,$$
$$h^{\mathrm{R}}_{(i+1/2)^-,j} = \eta^n_{i+1,j} - \frac{1}{2}\Phi\left(\eta^n_{i+2,j} - \eta^n_{i+1,j}\right) - z_{i,j}\,, \qquad h^{\mathrm{R}}_{(i+1/2)^+,j} = \eta^n_{i+1,j} - \frac{1}{2}\Phi\left(\eta^n_{i+2,j} - \eta^n_{i+1,j}\right) - z_{i+1,j}\,, \tag{10}$$

where Φ denotes a suitable limiter function enforcing the TVD constraint to prevent numerical oscillations at solution discontinuities [28, 42]. Similar reconstructions can be accomplished for the conserved variables $\overline{q}_x$ and $\overline{q}_y$. An estimate of the variable $\overline{h}$ at cell interfaces can then be derived from the geometrical properties of the adjacent cells. With reference to the example of Figures 3 and 4 with $H_{i,j} \to +\infty$:

$$\overline{h}^{\mathrm{L}}_{(i+1/2)^-,j} = h^{\mathrm{L}}_{(i+1/2)^-,j}, \qquad \overline{h}^{\mathrm{R}}_{(i+1/2)^-,j} = h^{\mathrm{R}}_{(i+1/2)^-,j},$$
$$\overline{h}^{\mathrm{L}}_{(i+1/2)^+,j} = \begin{cases} h^{\mathrm{L}}_{(i+1/2)^+,j} & \text{if } h^{\mathrm{L}}_{(i+1/2)^+,j} \le H_{i+1,j} \\ H_{i+1,j} + \left(\dfrac{T_x}{\Delta x} + \dfrac{T_y}{\Delta y} - \dfrac{T_x T_y}{\Delta x \Delta y}\right)\cdot\left(h^{\mathrm{L}}_{(i+1/2)^+,j} - H_{i+1,j}\right) & \text{if } h^{\mathrm{L}}_{(i+1/2)^+,j} > H_{i+1,j} \end{cases}, \tag{11}$$
$$\overline{h}^{\mathrm{R}}_{(i+1/2)^+,j} = \begin{cases} h^{\mathrm{R}}_{(i+1/2)^+,j} & \text{if } h^{\mathrm{R}}_{(i+1/2)^+,j} \le H_{i+1,j} \\ H_{i+1,j} + \left(\dfrac{T_x}{\Delta x} + \dfrac{T_y}{\Delta y} - \dfrac{T_x T_y}{\Delta x \Delta y}\right)\cdot\left(h^{\mathrm{R}}_{(i+1/2)^+,j} - H_{i+1,j}\right) & \text{if } h^{\mathrm{R}}_{(i+1/2)^+,j} > H_{i+1,j} \end{cases},$$

where the extrapolated variables at the intercell boundary $(i+1/2, j)^-$ are calculated on the basis of the geometry of the (i, j)-cell, whereas the extrapolated variables at the cell interface $(i+1/2, j)^+$ are computed by using the geometry of the $(i+1, j)$-cell (see Figure 3).

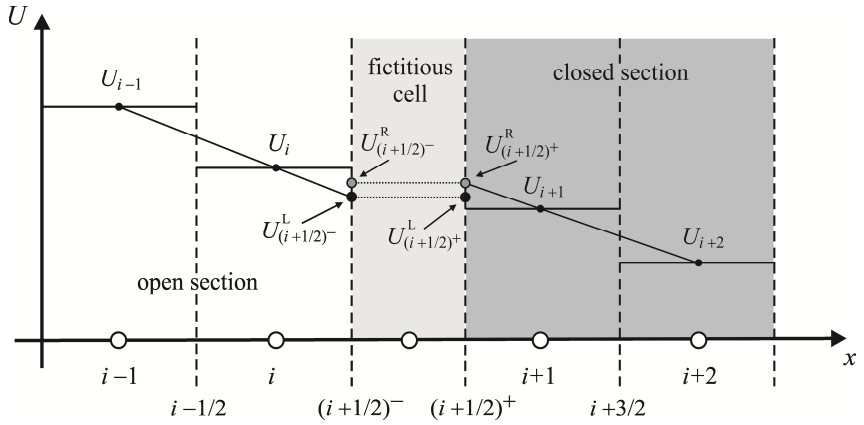

Figure 4. Linear one-sided MUSCL-Hancock extrapolation of intercell variables at a ceiling discontinuity.

The boundary extrapolated variables are then evolved over $\Delta t/2$ to achieve second-order accuracy in time. For an ordinary intercell not involving a top discontinuity, the evolution in time is performed according to the following expressions:

$$\overline{\mathbf{U}}^{\mathrm{L}}_{(i+1/2)^-,j} = \overline{\mathbf{U}}^{\mathrm{L}}_{(i+1/2)^+,j} = \mathbf{U}^{\mathrm{L}}_{(i+1/2)^-,j} - \frac{\Delta t}{2\Delta x}\left[\mathbf{F}\left(\mathbf{U}^{\mathrm{L}}_{(i+1/2)^-,j}\right) - \mathbf{F}\left(\mathbf{U}^{\mathrm{R}}_{(i-1/2)^+,j}\right)\right] - \frac{\Delta t}{2\Delta y}\left[\mathbf{G}\left(\mathbf{U}^{\mathrm{L}}_{i,(j+1/2)^-}\right) - \mathbf{G}\left(\mathbf{U}^{\mathrm{R}}_{i,(j-1/2)^+}\right)\right],$$
$$\overline{\mathbf{U}}^{\mathrm{R}}_{(i+1/2)^+,j} = \overline{\mathbf{U}}^{\mathrm{R}}_{(i+1/2)^-,j} = \mathbf{U}^{\mathrm{R}}_{(i+1/2)^+,j} - \frac{\Delta t}{2\Delta x}\left[\mathbf{F}\left(\mathbf{U}^{\mathrm{L}}_{(i+3/2)^-,j}\right) - \mathbf{F}\left(\mathbf{U}^{\mathrm{R}}_{(i+1/2)^+,j}\right)\right] - \frac{\Delta t}{2\Delta y}\left[\mathbf{G}\left(\mathbf{U}^{\mathrm{L}}_{i+1,(j+1/2)^-}\right) - \mathbf{G}\left(\mathbf{U}^{\mathrm{R}}_{i+1,(j-1/2)^+}\right)\right]. \tag{12}$$

Conversely, at an intercell characterized by a totally or partially submerged top discontinuity (see the (i+1/2, j)-interface in Figures 3 and 4), the evolved boundary variables $\overline{\mathbf{U}}^{\mathrm{L}}_{(i+1/2)^-,j}$ and $\overline{\mathbf{U}}^{\mathrm{R}}_{(i+1/2)^+,j}$ are still calculated according to Equation (12), whereas $\overline{\mathbf{U}}^{\mathrm{R}}_{(i+1/2)^-,j}$ and $\overline{\mathbf{U}}^{\mathrm{L}}_{(i+1/2)^+,j}$ are computed with reference to cells (i, j) and (i+1, j) respectively, namely:

$$\begin{aligned}
\overline{\mathbf{U}}^{\mathrm{R}}_{(i+1/2)^-,j} &= \mathbf{U}^{\mathrm{R}}_{(i+1/2)^-,j} - \frac{\Delta t}{2\Delta x}\left[\mathbf{F}\left(\mathbf{U}^{\mathrm{L}}_{(i+1/2)^-,j}\right) - \mathbf{F}\left(\mathbf{U}^{\mathrm{R}}_{(i-1/2)^+,j}\right)\right] - \frac{\Delta t}{2\Delta y}\left[\mathbf{G}\left(\mathbf{U}^{\mathrm{L}}_{i,(j+1/2)^-}\right) - \mathbf{G}\left(\mathbf{U}^{\mathrm{R}}_{i,(j-1/2)^+}\right)\right], \\
\overline{\mathbf{U}}^{\mathrm{L}}_{(i+1/2)^+,j} &= \mathbf{U}^{\mathrm{L}}_{(i+1/2)^+,j} - \frac{\Delta t}{2\Delta x}\left[\mathbf{F}\left(\mathbf{U}^{\mathrm{L}}_{(i+3/2)^-,j}\right) - \mathbf{F}\left(\mathbf{U}^{\mathrm{R}}_{(i+1/2)^+,j}\right)\right] - \frac{\Delta t}{2\Delta y}\left[\mathbf{G}\left(\mathbf{U}^{\mathrm{L}}_{i+1,(j+1/2)^-}\right) - \mathbf{G}\left(\mathbf{U}^{\mathrm{R}}_{i+1,(j-1/2)^+}\right)\right],
\end{aligned} \tag{13}$$

being in this case the flux component $[\mathbf{F}(\mathbf{U}^{\mathrm{L}}_{(i+1/2)^-,j})]_2$ suitably estimated in both Equations (12) and (13) by assessing the momentum term on the basis of the (i+1/2, j)$^+$ boundary values (differently from the pressure term).

Finally, the numerical fluxes are evaluated according to the classic FORCE method [42], by imposing the conditions of Equations (5)–(9) at a ceiling step discontinuity. In Equations (6) and (7), $h^{\mathrm{L}}_{(i-1/2)^-,j}$ is assumed as a simple and good estimate of $h_{i+1/2,j}$.

Theoretically, the numerical technique can also be applied where the ceiling of the closed structure varies gradually, thereby taking into account the pressure action in the planar directions of a converging or diverging top surface. Moreover, the presence of a bottom step can simultaneously be handled in an analogous manner.

Thanks to the inclusion of the dynamic load exerted by a structure deck on the flow, the numerical scheme is well-balanced at ceiling step discontinuities, since it rigorously satisfies the *C*-property regarding a stationary solution [46, 47], i.e. it is capable to preserve a static condition even when the closed structure runs partly or totally full.

2.4. Treatment of the friction term

The friction slopes in Equation (2) are assessed by means of the well-known Manning formula:

$$S_{\mathrm{fx}} = \frac{n_{\mathrm{fx}}^2 u\sqrt{u^2+v^2}}{\overline{h}_x^{4/3}}, \qquad S_{\mathrm{fy}} = \frac{n_{\mathrm{fy}}^2 v\sqrt{u^2+v^2}}{\overline{h}_y^{4/3}}, \tag{14}$$

where n_{fx} and n_{fy} are directional Manning coefficients, while u and v are the velocity components in the x and y-axis directions, respectively, which can be easily estimated from the unit discharges $\overline{q}_x$ and $\overline{q}_y$.

Commonly, n_{fx} and n_{fy} are assumed equal, and suitable values are chosen depending on the bed roughness. However, for flows through bridges, culverts, or others closed structures, in addition to the bottom friction the model should incorporate the resistance effect of lateral and top walls, especially when the structure is quite long and the flow section is narrow. For this purpose, a composite Manning coefficient is computed for each computational cell as a suitable combination of the resistance factors n_{b}, n_{w}, and n_{c} of the bottom, lateral walls, and ceiling, respectively, and then

equivalently assigned to the bottom. According to the classic Horton-Einstein methodology [37], the composite directional Manning coefficients can be defined as:

$$n_{\mathrm{fx}} = \left(\frac{n_{\mathrm{b}}^{3/2}\,\Delta y + n_{\mathrm{w}}^{3/2}\,\varsigma + n_{\mathrm{c}}^{3/2}\,\Delta y}{\Delta y} \right)^{2/3}, \qquad n_{\mathrm{fy}} = \left(\frac{n_{\mathrm{b}}^{3/2}\,\Delta x + n_{\mathrm{w}}^{3/2}\,\varsigma + n_{\mathrm{c}}^{3/2}\,\Delta x}{\Delta x} \right)^{2/3} \tag{15}$$

in which ς is equal to the piezometric head h if $h < H$, whereas it is equal to the top height H if $h \geq H$. Obviously, n_{w} and n_{c} must be set to zero if no lateral or top walls are present, and $n_{\mathrm{c}} = 0$ when the closed structure does not run full locally, i.e. when $h < H$.

Finally, it is worth noticing that the explicit inclusion in the momentum balance of the dynamic action exerted by the structure deck on the flow prevents having to add local energy losses in the source term at the entrance and exit of the structure. These internal energy losses can then be derived from model results.

3. VALIDATION OF THE MODEL

In this section numerical results are compared with both analytical solutions of 1D Riemann problems with a ceiling step discontinuity and experimental data of steady and unsteady mixed flows available in literature, in order to verify the capability and accuracy of the method.

3.1. 1D test cases with analytical solution

This subsection deals with 1D Riemann problems with a discontinuous top surface. The discontinuous initial-value problem for a 1D shallow water mixed flow on a horizontal frictionless bed was analyzed by Maranzoni et al. [19]. A ceiling vertical step is introduced here at the same location as the flow state discontinuity. Accordingly, the following condition on the top function H:

$$H(x,t) = \begin{cases} H_{\mathrm{L}} & \text{for } x < 0 \\ H_{\mathrm{R}} & \text{for } x > 0 \end{cases} \tag{16}$$

is coupled with the piecewise constant initial data

$$\mathbf{U}(x,0) = \begin{cases} \mathbf{U}_{\mathrm{L}} & \text{for } x < 0 \\ \mathbf{U}_{\mathrm{R}} & \text{for } x > 0 \end{cases}. \tag{17}$$

It must be noted that this is a purely theoretical situation, since the flow cannot actually be considered shallow near a sharp vertical variation of the flow geometry.

Firstly, a strategy for building the exact solution of this special Riemann problem must be devised. The solution of the standard Riemann problem for the 1D free surface shallow water equations is known to be self-similar (indeed it depends on the variable x/t only) and consists of two elementary waves (namely shocks or rarefactions) associated with the two characteristic speeds λ_1 and λ_2 ($> \lambda_1$) of the system of equations, separated by an intermediate *star region* where

the flow state is constant in time [28, 43]. However, by extending the similarity considerations made by Alcrudo and Benkhaldoun [38] for the case of a Riemann problem with a bottom step, the presence of the discontinuity in the top function H can be expected to induce the formation of two distinct intermediate states $\mathbf{U}_L^*$ and $\mathbf{U}_R^*$ in the *star region* on the left- and the right-hand side of the discontinuity position ($x = 0$), respectively. Therefore, if the case in which a rarefaction wave spreads across the ceiling step discontinuity is excluded, the solution of this modified Riemann problem can be symbolically represented by the following diagram:

$$\mathbf{U}_L \xrightarrow{W^1} \mathbf{U}_L^* \xrightarrow{SC} \mathbf{U}_R^* \xrightarrow{W^2} \mathbf{U}_R\,, \tag{18}$$

in which the left wave W^1 (associated with the characteristic speed λ_1) connects the flow states $\mathbf{U}_L$ and $\mathbf{U}_L^*$, and the right wave W^2 (associated with λ_2) similarly connects the states $\mathbf{U}_R^*$ and $\mathbf{U}_R$, whereas $\mathbf{U}_L^*$ and $\mathbf{U}_R^*$ are conjugate states across the top surface step discontinuity through a suitable steady connection (SC). Figure 5a shows the corresponding wave pattern in the x-t plane for the case of a left rarefaction R^1 and a right shock S^2.

The centred rarefaction wave is known to link two flow states by means of a smooth transition and the Riemann invariant to be constant across this wave [28, 43]. For the left rarefaction R^1 of Figure 5a, the 1-Riemann invariant reads: $u + \omega$, where ω denotes the Escoffier stage variable [48], thus the flow states $\mathbf{U}_L$ and $\mathbf{U}_L^*$ at the head and tail of the wave, respectively, are related as follows:

$$u_L^* = u_L + (\omega_L - \omega_L^*)\,. \tag{19}$$

Since ω is defined as [48]:

$$\int_0^h \sqrt{g\frac{B(\xi)}{A(\xi)}}\mathrm{d}\xi\,, \tag{20}$$

with B and A being the cross-section width and area at depth ξ, respectively, it derives that $\omega = 2(gh)^{1/2}$ for a rectangular open channel cross-section and that:

$$\begin{cases} \omega = 2\sqrt{gh} & \text{for } h < H \\ \omega = 2\sqrt{gH}\left\{1+\sqrt{\frac{b}{T}}\left[\sqrt{1+\frac{T}{b}\left(\frac{h}{H}-1\right)}-1\right]\right\} & \text{for } h \geq H \end{cases} \tag{21}$$

for a rectangular closed channel with width b and height H in which a narrow slot of width T is added on the top. Equation (19) defines a one-parameter set of flow states which can be connected to $\mathbf{U}_L$ through R^1. In Figure 5b, this family of states is described by a R^1-integral curve plotted in the u-h phase plane for the exemplifying case of Test 1 (see Table I) in which the left wave is a classic free surface rarefaction. A similar definition can be given of the integral curve for a right rarefaction along which the 2-Riemann invariant is constant.

With regard to the shock wave, it is a well-known fact that the Rankine-Hugoniot condition must be satisfied across the discontinuity [28, 43]. For the right shock S^2 in the wave pattern of Figure 5a, this condition leads to the following two relations between the flow states $\mathbf{U}_R^*$ and $\mathbf{U}_R$:

$$c = \frac{A_R u_R - A_R^* u_R^*}{A_R - A_R^*}, \tag{22}$$

$$u_R^* = u_R + \sqrt{g\left(1 - \frac{A_R}{A_R^*}\right)\left(\zeta_{GR}^* \frac{A_R^*}{A_R} - \zeta_{GR}\right)}, \tag{23}$$

in which c is the shock speed, A and u are the flow area and the cross-sectional velocity, respectively, and ζ_G is the vertical distance of the flow area's centroid from the water surface. Obviously, for a rectangular open channel of width b, $A = bh$ and $\zeta_G = h/2$; for a closed rectangular section with a Preissmann slot on the top, the geometric relations can easily be extended beyond the crown. Therefore,

$$\begin{cases} A = bh & \text{for } h < H \\ A = bH\left[1 + \frac{T}{b}\left(\frac{h}{H} - 1\right)\right] & \text{for } h \geq H \end{cases} \quad \text{and} \quad \begin{cases} \zeta_G A = \frac{bh^2}{2} & \text{for } h < H \\ \zeta_G A = \frac{bH^2}{2}\left[2\frac{h}{H} - 1 + \frac{T}{b}\left(\frac{h}{H} - 1\right)^2\right] & \text{for } h \geq H \end{cases}. \tag{24}$$

Equation (23) provides a one-parameter family of flow states potentially connected to $\mathbf{U}_R$ through S^2, which is represented by a S^2 Hugoniot locus in the u-h phase plane, as shown in Figure 5b for Test 1 (see Table I) in which the right wave is a pressurization shock moving downstream. The physically acceptable portion of this curve is the one which satisfies the entropy condition. A similar analysis can be performed for a left shock wave with suitable modifications.

In order to connect the flow variables $\mathbf{U}_L^*$ and $\mathbf{U}_R^*$ across the cross-section discontinuity at $x = 0$, both the mass-momentum and mass-energy approaches can theoretically be adopted. To deal with the similar case of the Riemann problem with a bottom step, Alcrudo et Benkhaldoun [38] adopted the mass-energy approach, whereas Rosatti and Begnudelli [35] used the mass-momentum approach. The latter is applied here to avoid having to add internal energy losses to the source term of the equations, and estimate head loss model parameters which would be difficult to calibrate. Accordingly, the application of the mass conservation principle across the top surface discontinuity leads to:

$$A_L^* u_L^* = A_R^* u_R^*. \tag{25}$$

Moreover, for the case of the negative step of Figures 2-4 (which typically occurs at the entrance of the closed structure), if the total pressure force exerted by the vertical surface of the structure is assumed to be equal to the hydrostatic force calculated below the upstream piezometric surface [49], the momentum equation across the ceiling discontinuity becomes

$$g\zeta_{GL}^* A_L^* + u_L^{*2} A_L^* = g\zeta_{GR}^* A_R^* + u_R^{*2} A_R^* + \frac{1}{2} g (h_L^* - H)^2 b. \tag{26}$$

Similar relations can be written for a positive step (at the exit of the structure) and for a submerged step of finite height. Equations (25) and (26) characterize the steady connection (SC) between the two conjugate states $\mathbf{U}_L^*$ and $\mathbf{U}_R^*$ in the *star region* and allow determining one of the two adjacent states when the other is known. For the example of the wave

pattern in Figure 5a, the two intermediate states $\mathbf{U}_L^*$ and $\mathbf{U}_R^*$ can then be calculated numerically by solving the system of Equations (19), (23), (25), and (26). Figure 5b shows the graphical solution of the problem in the *u*-*h* plane for the case of Test 1 described in Table I. Actually, equations (25) and (26) provide a one-parameter family of flow states joined to the integral curve R^1 across the steady connection SC (see the SC(R^1) curve in the *u*-*h* plane of Figure 5b) and, at the same time, provide a one-parameter family of states joined to the Hugoniot locus of S^2 (see the SC(S^2) curve in Figure 5b). Based on the sketch of Equation (18), the state $\mathbf{U}_R^*$ is obtained by intersecting the S^2 Hugoniot locus with the SC(R^1) curve, whereas the state $\mathbf{U}_L^*$ is obtained as an intersection between the R^1 integral curve and the SC(S^2) curve (Figure 5b). The same strategy can be applied for different combinations of elementary waves with obvious adaptations.

Finally, the structure of the solution through any rarefaction can be derived from the well-know theory concerning the rarefaction waves [28, 43].

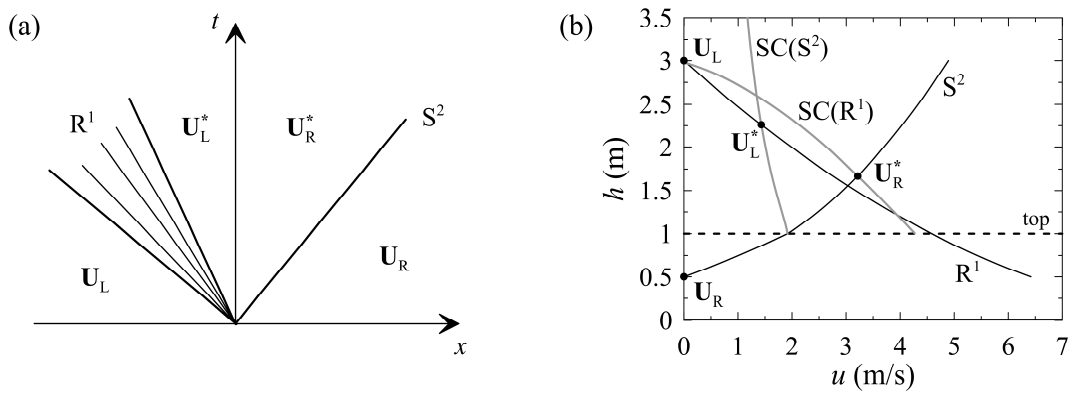

Figure 5. a) Wave pattern in the *x*-*t* plane of the general solution of the 1D Riemann problem with a ceiling step discontinuity at $x = 0$ (case of a left rarefaction and a right shock). b) Example of solution of the Riemann problem in the *u*-*h* phase plane (Test 1 of Table I).

Five examples are considered in the following in order to represent a few possible and significant situations characterized by different combinations of allowed wave patterns, including transitions between free surface and pressurized regimes. The flow field is [−5, 5] m × [0, 1] m, and the test conditions are listed in Table I.

Table I. Test conditions for five Riemann problems with a ceiling step discontinuity.

Test	h_L (m)	u_L (m/s)	h_R (m)	u_R (m/s)	H_L (m)	H_R (m)	Description
1	3.0	0.0	0.5	0.0	+∞	1.0	Left free surface rarefaction and right transitional shock
2	3.0	0.0	1.5	0.0	+∞	1.0	Left free surface rarefaction and right positive pressure wave
3	3.0	0.0	1.5	0.0	2.0	1.0	Left negative pressure wave and right positive pressure wave

4	0.9	1.5	0.9	0.0	$+\infty$	1.0	Left free surface shock and right transitional shock
5	3.0	0.0	1.5	0.0	1.0	$+\infty$	Left negative pressure wave and right free surface shock

For the numerical simulations, the computational domain is discretized by means of square cells sized $\Delta x = \Delta y = 0.01$ m and the Courant number Cr is set at 0.7. The dimensionless slot width is set equal to 0.01 in the flow direction ($T_y/\Delta y = 10^{-2}$), while it is assumed some order of magnitude smaller in the transverse direction ($T_x/\Delta x = 10^{-6}$). The ratio of the slot width on the transverse pipe/channel dimension is commonly set at 0.01 in the practice (e.g. [21], [23], [50]), as it guarantees a good compromise between accuracy, numerical stability, and computational efficiency in predicting the propagation of transitional bores [19]. However, the specific value of this model parameter is irrelevant for the validation performed here, provided that numerical and exact solutions are obtained consistently with the same longitudinal slot width. The transverse slot is set much narrower than the longitudinal one, due to the 1D character of the tests and the need to limit the fictitious increment of the water volume which can be stored in the conduit. The sensitivity analysis carried out by Maranzoni et al. [19] has shown that in 1D problems the dimensionless width of the transverse slot should be set at least one/two orders of magnitude lower than the dimensionless width of the longitudinal slot in order to accurately describe the propagation of transitional shocks.

Numerical water depth and x-velocity profiles at selected times are reported in Figure 6. In general, analytical solutions and numerical results agree, both for inlet (Tests 1-4) and outlet (Test 5) cases. In particular, shocks and rarefactions are well reproduced, as well as the transitions between free surface and pressurized flow (see the pressurization shock waves travelling to the right in Tests 1 and 4). However, very small spurious oscillations arise in the pressure head profiles of Tests 1 and 4 at the conduit-filling bores. This may be due to the fact that, despite the application of slope limiter functions, the numerical method introduces an insufficient amount of numerical viscosity around sudden flow regime transitions, where an abrupt change occurs in the wave celerity [51, 52]. The flow state discontinuity at $x = 0$ is correctly predicted and no unphysical oscillations appear at this location. It must be noticed that the accuracy in the prediction of the flow state discontinuity depends on the goodness of the numerical estimate of the water pressure force exerted by the deck surface on the flow. Although the steady jump in water depth at $x = 0$ is very small in Tests 2, 3, 4, and 5, it is captured by the numerical model (see, as an example, the inset in the left-hand side panel concerning Test 4 in Figure 6). In Test 3, the step in the top function has a finite height and the flow is surcharged everywhere with a negative pressure wave travelling to the left and a positive pressure wave moving to the right. The water flow force on the deck surface can easily be predicted from the computed water depth profile on the basis of the shallow water assumption as the total hydrostatic thrust exerted below the water surface. For example, in Test 1 the pressure force predicted on the deck surface is equal to $7.73 \cdot 10^3$ N per unit length.

Figure 7 compares analytical and numerical profiles of unit discharge and total head for Test 1 at a selected time (t = 0.5 s). Figure 7a shows that the equilibrium condition prescribed by the continuity equation on the flow discharge is well preserved across the ceiling step, despite the appearance of a single outlier just at the discontinuity site. Figure 7b confirms that the numerical model intrinsically introduces energy losses at abrupt changes in the top elevation.

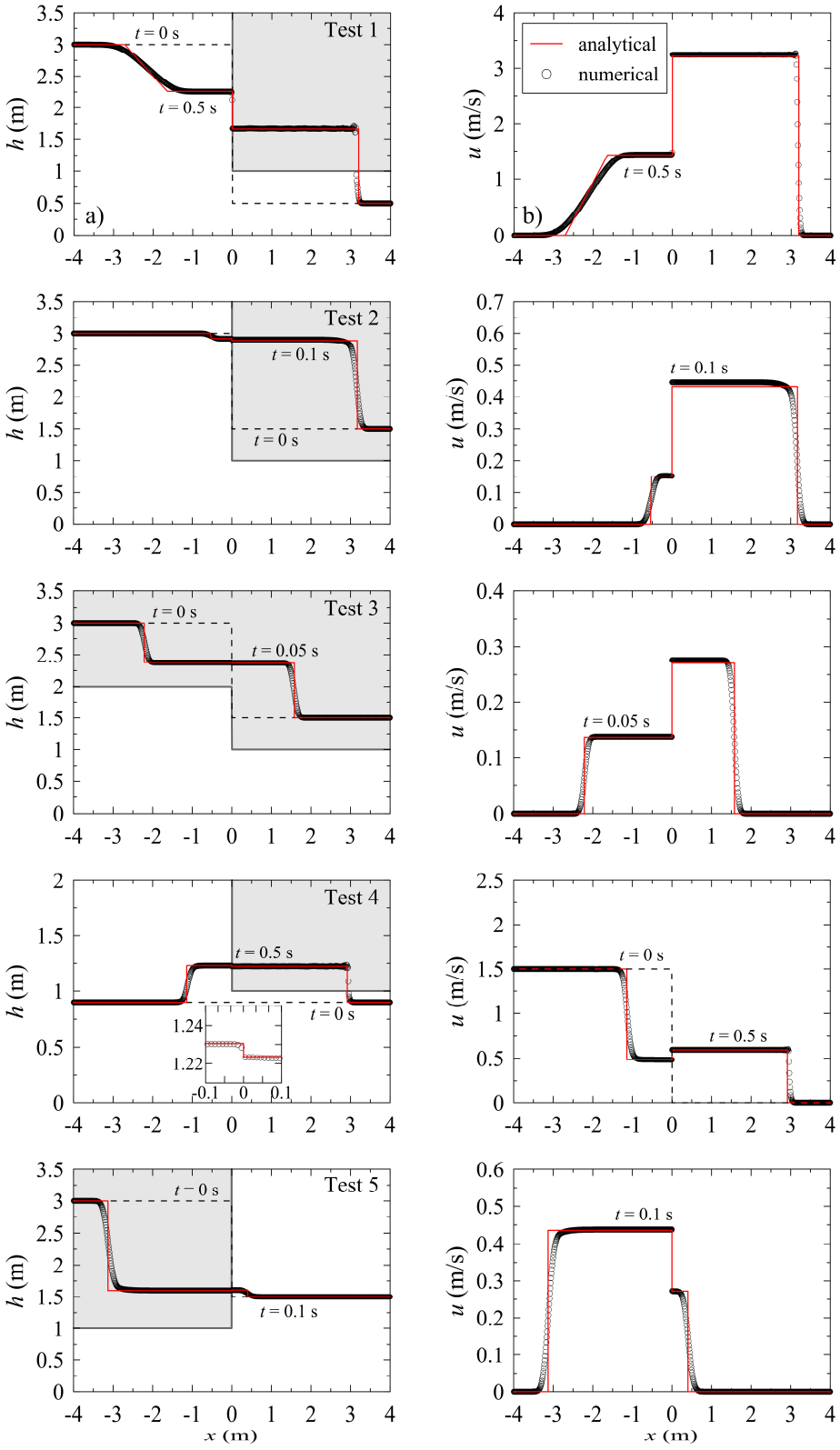

Figure 6. Comparison between analytical solutions and numerical results at different times for the test cases of Table I: a) pressure head; b) velocity (Δx = 0.01 m, Δy = 0.01 m, $T_y = \Delta y/10^2$, $T_x = \Delta x/10^6$, Cr = 0.7).

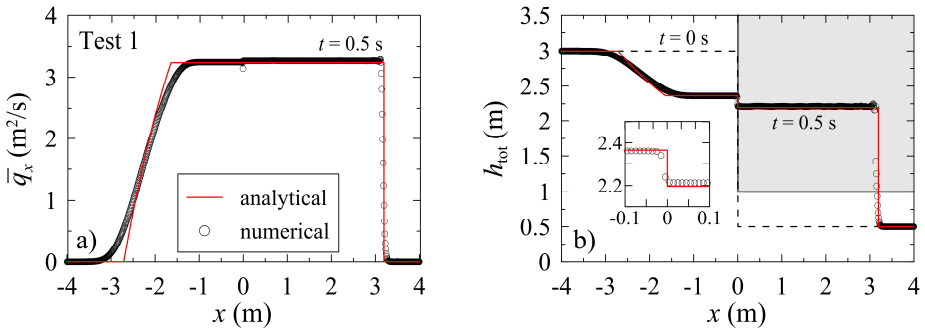

Figure 7. Comparison between analytical and numerical unit discharge (a) and total head (b) profiles at a selected time for Test 1 (Δx = 0.01 m, Δy = 0.01 m, $T_y = \Delta y/10^2$, $T_x = \Delta x/10^6$, Cr = 0.7).

3.2. Experimental 1D steady test cases

In this subsection, numerical results are compared with some experimental data acquired by Ratia et al. [18] during a laboratory investigation carried out in a 6 m long and 24 cm wide rectangular horizontal flume, orthogonally crossed by a bridge. Various model bridge shapes were considered, and different subcritical steady state flows were realized by changing the flow discharge. The bridge was partly or totally under pressure, depending on the tailwater depth. The water height was measured at two gauge points located 1 m upstream and 3 m downstream of the bridge axis, respectively, along the channel centerline. Only the tests concerning a beam bridge with 3 cm opening height w are considered here. The corresponding test conditions are detailed in Table II. In the tests selected the experimental obstruction ratio (defined as $(h_u - w)/h_u$, with reference to the upstream water depth h_u) ranges from 0.19 to 0.51, and the beam bridge acts as a drowned sluice gate, with downstream Froude number ranging between 0.74 and 0.81.

These test cases are useful to analyze the model's ability to introduce a suitable amount of local energy dissipation and consequently to reliably predict the backwater effect induced by crossing structures, which is one of the most important aspects in practical applications.

A 5.8 m channel reach limited by the downstream measuring cross-section is considered as computational domain, which is discretized by means of square cells sized $\Delta x = \Delta y$ = 0.01 m. The dimensionless slot width $T_y/\Delta y$ in the flow direction is assumed equal to 0.01, while it is assumed one order of magnitude smaller in the transverse direction ($T_x/\Delta x$ = 0.001). Friction resistance is computed by setting the Manning's roughness coefficient at 0.011 $m^{-1/3}s$ for both bed and ceiling surfaces, whereas friction at lateral walls is neglected. The constant water level measured at the downstream gauge point is imposed at the outlet boundary and the inflow discharge is specified at the upstream boundary of the domain. The Courant number is set at 0.7.

Some significant numerical results are reported in the two last columns in Table II. The calculated backwater effect is underestimated compared to the measured one, with increasing error for higher water stages. This means that the numerical model introduces an insufficient amount of energy loss at the vertical flow constriction induced by the bridge. Actually, the flow through a bridge is generally rapidly varied in space, thus the shallow water approximation is inadequate to model the significant vertical accelerations involved, especially for high water stages. To overcome this limitation, the Manning coefficient n_c at the lower surface of the bridge can be regarded as a model parameter and suitably calibrated. As an example of the use of numerical results to obtain design information of practical interest, Table II also reports the predicted drag coefficient C_D, which is defined as [12]:

$$\frac{F_D}{0.5\rho(h_u - w)u_u^2}, \tag{27}$$

where F_D is the drag force on the bridge per unit length, ρ the density of water, and u_u the approaching flow velocity at the upstream measuring section. The drag force on the bridge is computed by applying the momentum principle in the longitudinal direction to a suitable channel reach including the bridge [11]. In the application presented here, the channel reach considered as a control volume is enclosed between two cross-sections located 6 cm upstream and 6 cm downstream of the entrance and exit of the bridge, respectively.

Table II. Test conditions and numerical results for some selected steady flow experiments concerning a beam bridge (Ratia et al. [18]).

Test	Flow discharge Q (l/s)	Downstream water depth h_d (m)	Downstream Froude number Fr_d (-)	Upstream water depth h_u (m)	Obstruction ratio $(h_u - w)/h_u$ (-)	Measured backwater $h_u - h_d$ (m)	Predicted backwater $h_u - h_d$ (m)	Computed drag coefficient C_D (-)
a	2.500	0.027	0.75	0.037	0.19	0.010	0.0086	0.150
b	3.056	0.031	0.74	0.042	0.29	0.011	0.0090	0.243
c	3.583	0.033	0.80	0.048	0.38	0.015	0.0105	0.346
d	4.139	0.036	0.81	0.054	0.44	0.018	0.0115	0.496
e	4.722	0.040	0.79	0.058	0.48	0.018	0.0120	0.715
f	5.083	0.041	0.81	0.061	0.51	0.020	0.0135	0.889

3.3. Experimental 2D steady test case

In this subsection the numerical model is applied to one of the experimental test cases by Van Nam. et al. [41] concerning steady mixed flows through a culvert. The laboratory set-up is sketched in Figure 8 and consists of a 10.4 m long and 0.98 m wide rectangular flume with horizontal bottom in which a 2 m long, 0.2 m wide, and 0.15 m high box culvert is inserted asymmetrically. As the culvert is placed as adherent to the right-hand side wall of the flume, the flow

forced to pass through the culvert is expected to show marked 2D planar features, especially near both the entrance and the exit of the conduit. For this reason, these experimental tests can be suitable to assess the ability of the model to reproduce 2D flow fields caused by crossing structures (potentially flowing partly or totally full) and to predict the induced backwater effect.

Various subcritical steady flow conditions were realized by changing the flow discharge and adjusting the water depth at the downstream end of the flume, but in all the experimental tests the outlet of the culvert was submerged and the culvert ran full. The water height and the planar velocity components were measured at some gauge points in the open-channel stretches upstream and downstream of the structure, whereas pressure measurements were performed inside the culvert. Only the test characterized by 10.1 l/s flow discharge and 0.31 m water level at the downstream boundary is considered here.

The computational domain is discretized by means of square cells sized $\Delta x = \Delta y = 0.005$ m and the dimensionless slot widths are assumed equal to 0.01 in both the longitudinal and transverse direction. The Manning's roughness coefficient is set at 0.011 $m^{-1/3}s$ at the channel bottom, while friction at the side walls of the flume is neglected. Conversely, the roughness coefficients of the left-hand side wall and the top of the culvert (which were made of a different material than the flume's side walls) are set at 0.011 $m^{-1/3}s$. Finally, the Courant number is assumed equal to 0.7. As an example of the results obtained by the numerical simulation, Figure 9 shows the piezometric head contour map (Figure 9a) and the vector map of the velocity field superimposed on the velocity magnitude contour map (Figure 9b) for a channel stretch including the culvert.

Figure 10 shows a comparison between numerical results and experimental data. In particular, Figure 10a compares predicted and measured water surface profiles along the culvert centerline (Section L in Figure 8). The backwater effect is well reproduced, even if it is slightly overestimated as well as the piezometric head profile of the surcharged flow through the closed conduit. On the contrary, the local drop in piezometric head at the entrance of the culvert is not captured by the numerical model. Indeed, the flow constrained to enter a submerged culvert is rapidly varied in space at the inlet, with significant vertical accelerations which cannot be modeled when adopting the shallow water approximation. Figure 10b shows numerical and experimental profiles of both x- and y-velocity components at transverse Section U located just upstream of the culvert entrance (see Figure 8). The numerical model correctly predicts the increase in the longitudinal velocity u at the culvert inlet caused by the sudden reduction in the channel cross-section. The transverse velocity v assumes very small values at Section U, and negative values before the inlet are consistent with the flow concentration towards the culvert. The positive value of v measured at Section U away from the culvert entrance seems to suggest the development of an eddy zone near the corner on the left-hand side of the upstream reach of the flume. This flow feature is not reproduced by the numerical model. Figure 10c compares numerical and experimental velocity profiles at transverse Section D located just downstream of the pipe outlet (see again Figure 8).

The numerical model underestimates the velocity of the flow exiting from the culvert, even if it must be noticed that this specific measurement is claimed to be affected by high uncertainty (in the order of 0.10 m/s). On the other hand, the model captures the occurrence of positive values of transverse velocity at Section D induced by the expansion of the flow.

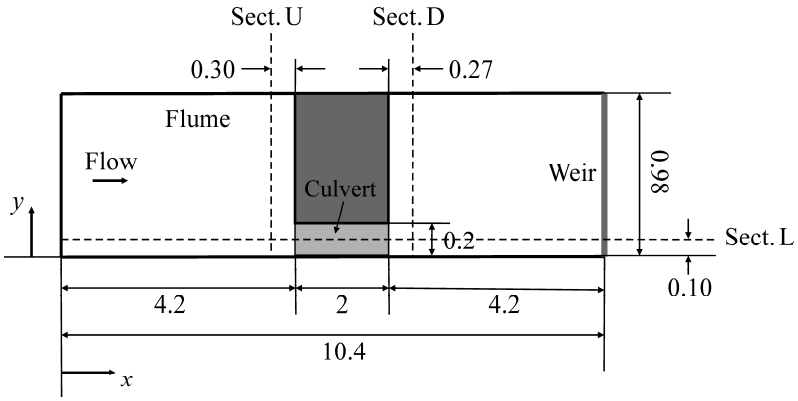

Figure 8. Plan view of the Van Nam et al.'s laboratory set-up [41] for the experimental investigation of steady 2D mixed flows (dimensions in m).

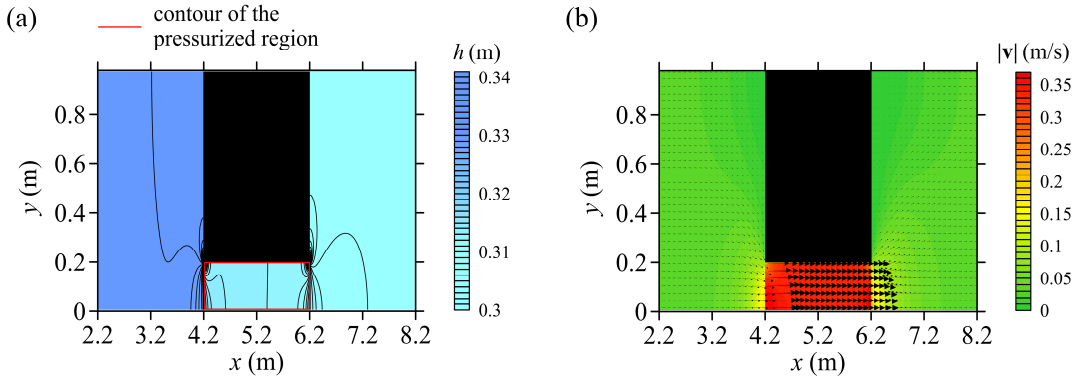

Figure 9. Steady test case by Van Nam et al. [41]: a) contour map of predicted piezometric heads, and b) numerical velocity field for a channel stretch including the culvert.

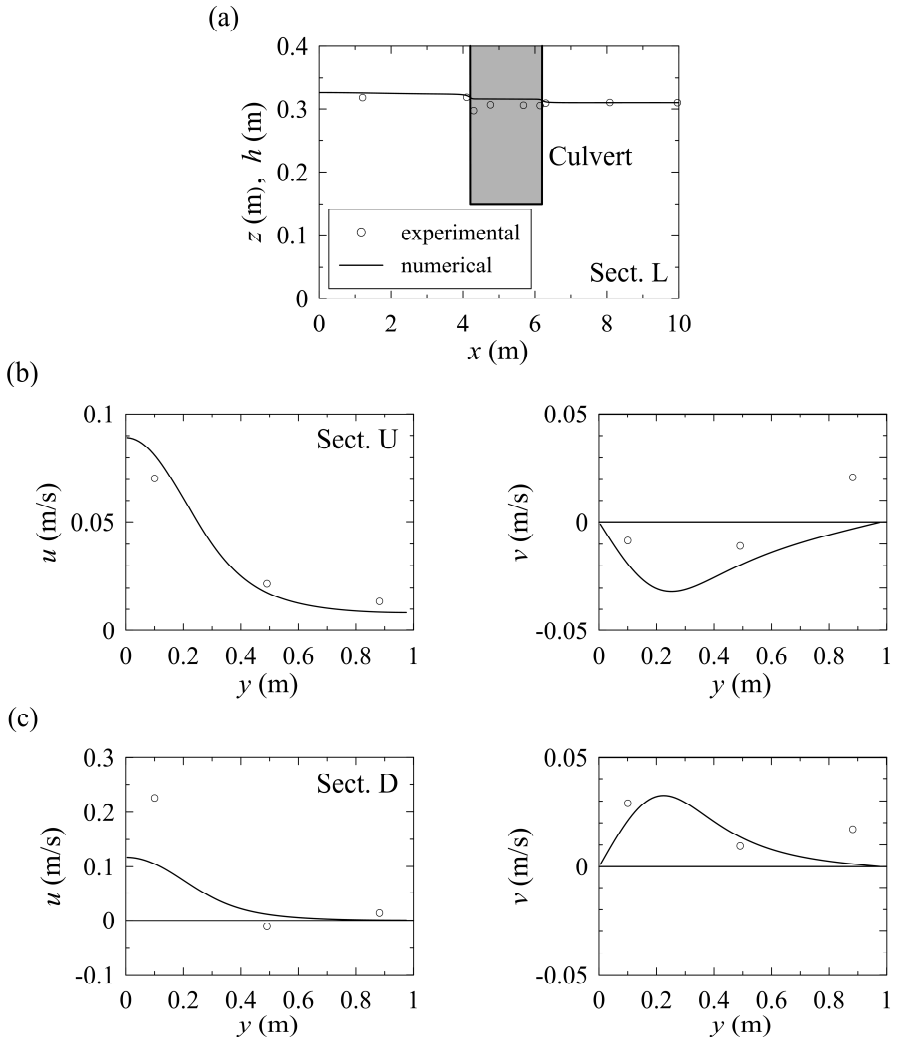

Figure 10. Steady test case by Van Nam et al. [41]: a) comparison between numerical and experimental piezometric head profiles along the culvert centerline; b) comparison of numerical and experimental *x*- and *y*- velocity components at two measuring sections.

3.4. Experimental dam-break test cases

Numerical simulations of dam-break flows through a bridge are presented in this subsection. The cases considered here are Tests no. 10 and 8 of the laboratory dam-break experiments carried out by Ratia et al. [18] in a 6.04 m long and 24 cm wide rectangular horizontal channel, connected by a 0.12 m high vertical bottom step to an upstream reservoir with planar dimensions 1.56 m × 0.84 m (Figure 11). The channel was orthogonally crossed by a bridge, and different bridge shapes and positions were investigated. In Test no. 10 the bridge was a 6 cm thick single-arch bridge with a semicircular opening of 7.5 cm radius and was located 1.646 m downstream of the channel inlet , whereas in Test no. 8 a 6 cm thick, triple-span beam bridge with 6 cm wide and 4.5 cm high openings was located 1.636 m from the channel inlet. A sluice gate was placed at the channel entrance, so that two different static water levels h_r and h_c could be imposed as initial condition in the head reservoir and in the channel, respectively. The sudden removal of the gate caused the formation of a bore which, propagating downwards into the flume, interfered with the bridge, even inducing its pressurization. The water height was measured by means of an imaging technique at two gauge points located at the

channel centerline, immediately upstream and downstream of the bridge (G_u and G_d, respectively). The test geometry and conditions are summarized in Figure 11 and Table III.

The computational domain is discretized by Cartesian cells sized $\Delta x = 0.005$ m × $\Delta y = 0.005$ m, and the dimensionless slot widths are assumed equal to 0.01 in both the longitudinal and transverse directions, due to the expected 2D character of the flow under the bridge. The Manning coefficient is set at 0.011 s $m^{-1/3}$ at the channel bottom, at the side walls of the channel, and at the low chord of the bridge. The bottom vertical step at the junction between the reservoir and the channel is treated according to the fictitious cell-based strategy described above. Moreover, the Courant number is set at 0.7.

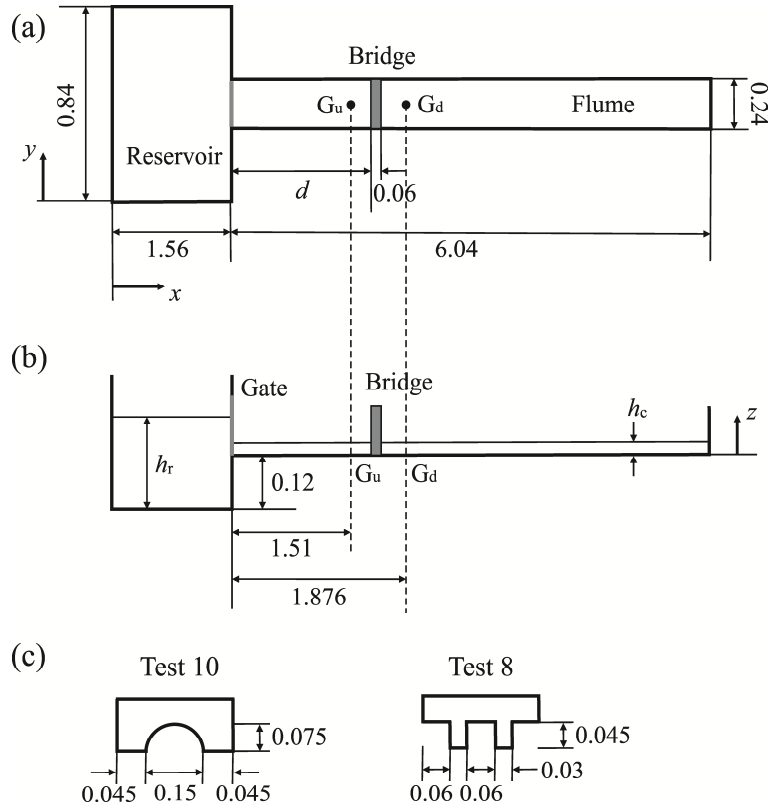

Figure 11. Sketch (not to scale) of the laboratory set up of the dam-break experiments by Ratia et al. [18]: a) plan view; b) longitudinal section; c) profiles of the bridge for Tests no. 10 and 8 (dimensions in m).

Table III. Test conditions of two selected laboratory dam-break test cases by Ratia et al. [18].

Test no.	Bridge type	d (m)	h_r (m)	h_c (m)
10	Single arch	1.646	0.180	0.011
8	Beam	1.636	0.180	0.009

Figure 12 shows some numerical results for Test 10 at $t = 2.5$ s, when the bore has already passed the obstruction and continues to move downwards, while a shock reflected by the bridge propagates upwards. The contour maps of the

computed water depths and velocity magnitudes reported in Figures 12a and b, respectively, depict the predicted 2D effects induced by the flow constriction in the vicinity of the bridge. The flow is rapidly varied under the bridge and, once it has passed through the constriction, gradually expands giving rise to two separation zones behind the bridge piers close to the side walls of the flume. Figure 12c shows the water surface longitudinal profile along the channel centerline at the same selected time. The central portion of the flow accelerates with a marked drawdown of the water surface, whereas at the outer boundaries the flow decelerates because of the lateral contraction. In the case considered, the contraction induces the transition from subcritical to supercritical flow, and a hydraulic jump occurs downstream of the bridge. Moreover, a pronounced backwater effect extends upstream of the bridge with a moving front. Finally, Figure 12d shows the computed cross-sectional profile along the bridge axis at $t = 2.5$ s. At this time, as a result of the transit of the bore, the bridge opening is partly full and the arched low chord is wet only on a short lateral portion.

Figure 13 compares experimental and numerical water depth time series for the two measuring points G_u and G_d indicated in Figure 11. With regard to gauge point G_u (Figure 13a), the arrival time of the downstream moving shock generated by suddenly removing the gate is well predicted; on the contrary, the increase in water depth caused by the presence of the obstruction is slightly overestimated. The reduction phase of the backwater effect appears more rapid in the numerical simulation than in the observations, but in any case the model provides a good reproduction of the experimental hydrograph's long-time behaviour. For gauge point G_d (Figure 13b), the numerical and measured water depth time series do not agree so well. Not only is the bore's arrival time slightly underestimated by the numerical model, the very complex flow pattern which develops in the wake behind the bridge induces oscillatory effects which affect the predicted water depth time series at G_d. Indeed, G_d is located near the hydraulic jump and a small displacement of this gauge point results in a significant variation of the computed water depth hydrograph. Finally, the height of the shock reflected by the downstream wall of the flume is well predicted, even if the wave celerity is slightly overestimated.

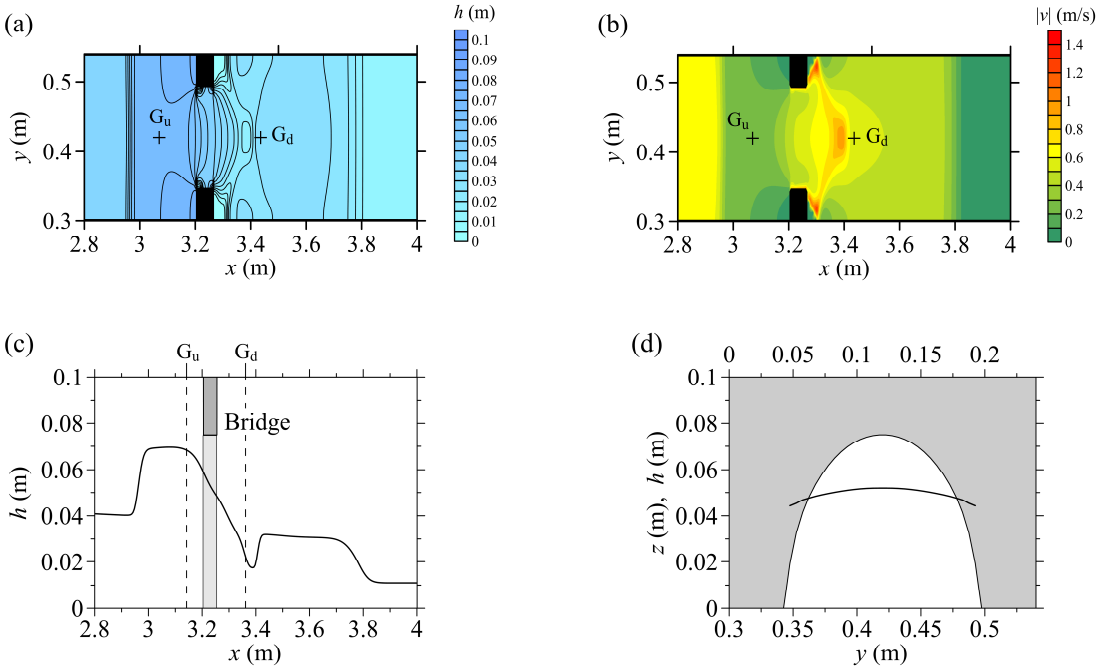

Figure 12. Example of numerical results obtained at t = 2.5 s around the arch bridge for the laboratory test case by Ratia et al. [18]: a) contour map of piezometric head with reference to the channel bottom, b) contour map of velocity magnitude, c) water depth longitudinal profile along the channel centerline, and d) piezometric head cross-sectional profiles along the bridge axis.

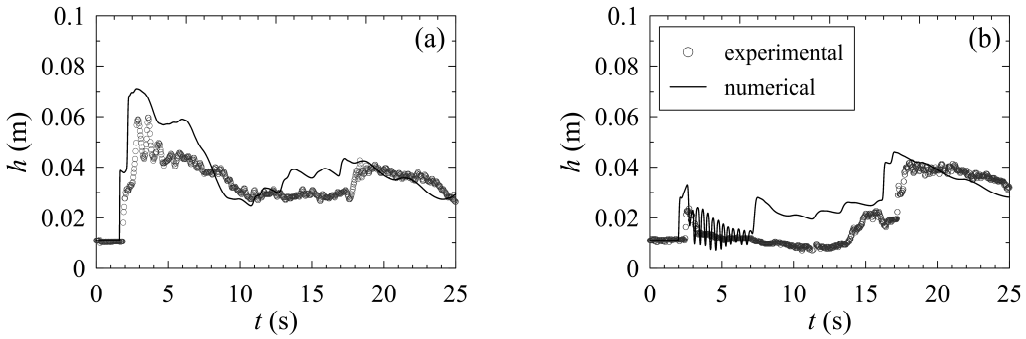

Figure 13. Comparison between experimental and numerical water depth time series for Test 10 by Ratia et al. [18]: a) upstream observation point G_u; b) downstream observation point G_d.

Similar comments can be made on the comparison between measured and predicted water depth time series at the same observation points G_u and G_d for Test 8 by Ratia et al. [18] (Figure 14). The peak of the water depth hydrograph at G_u is again overestimated by the numerical model, while the wave reflected by the bridge arrives at G_u earlier compared to the experiment (Figure 14a). Moreover, the numerical model tends to overestimate water levels at G_d and predicts shorter arrival times for both the bore coming from upstream, and the bore reflected by the downstream wall of the flume (Figure 14b).

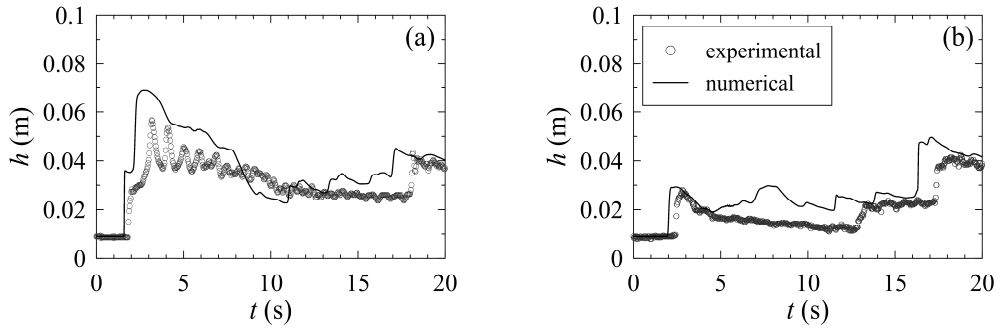

Figure 14. Comparison between experimental and numerical water depth time series for Test 8 by Ratia et al. [18]: a) upstream observation point G_u; b) downstream observation point G_d.

4. APPLICATION OF THE MODEL

In this section the numerical model is applied to an imaginary real-scale case concerning the transit of a fast flood wave through a multiple arch bridge. Figure 15 shows the geometry of the case study, which consists of a 200 m long straight channel with a 0.5% bottom slope and a 54 m wide rectangular cross-section. The channel is normally crossed by a 12 m wide multiple-span arch bridge with five openings formed by four 1 m thick piers parallel to the flow direction, with square noses and tails. Each opening is characterized by a 10 m span and by an arched low chord with a 6.85 m curvature radius and a 4.67 m key brick elevation with reference to the channel bottom. Two control cross-sections (S1 and S2 in Figure 15) and two observation points (G1 and G2) are considered just upstream and downstream of the bridge. Despite its simple geometry, this imaginary case study is a valid schematization of a real situation, and thus can be useful to evaluate the model's effectiveness and robustness in real-field applications.

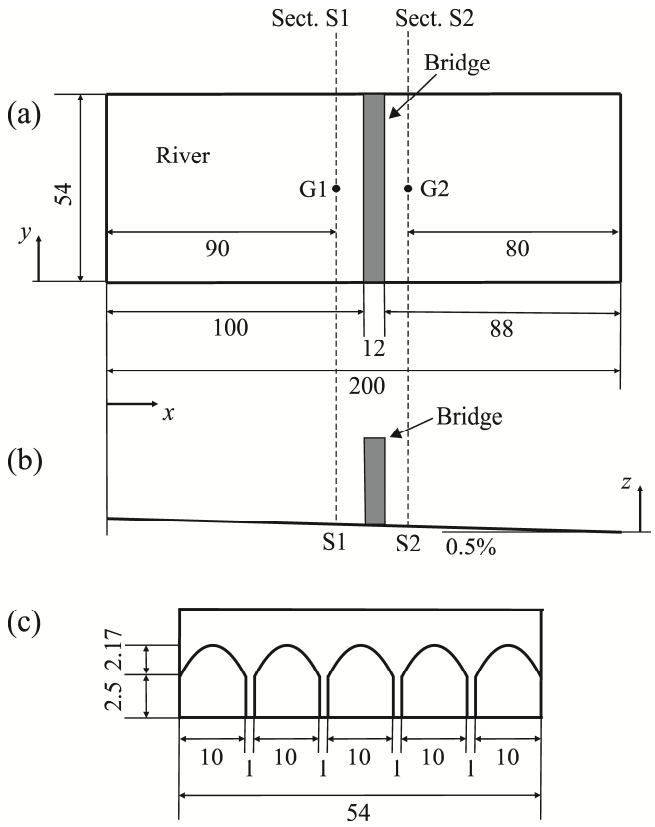

Figure 15. Sketch of the imaginary real-field case study: a) plan view; b) longitudinal section; c) profile of the bridge (dimensions in m).

The numerical simulation is performed on a Cartesian mesh with cell size Δx = 2 m × Δy = 0.25 m and dimensionless slot widths $T_y/\Delta y$ = 0.01 and $T_x/\Delta x$ = 0.001. The Manning coefficient is assumed equal to 0.04 s $m^{-1/3}$ at the channel bottom, as well as at the vertical walls of the piers and at the low chord of the bridge. A triangular shaped discharge hydrograph with a 1 h total duration and a 870 m^3/s peak discharge after 20 min is specified at the upstream boundary of the computational domain, whereas a transmissive condition is imposed at the downstream outlet. The steady state numerical solution obtained for a 50 m^3/s discharge is used as initial condition. Finally, the Courant number is set at 0.9. Figure 16 shows an example of numerical results obtained from the simulation. Figures 16a, b, d, and e refer to the time t = 30 min, during the first instants of the flood's falling stage, when the bridge openings run partially full. The presence of the bridge causes a sudden reduction in the channel cross-section, thus inducing significant 2D planar effects in the near-field (Figure 16a-b). The flow through the constriction is subcritical during the transit of the flooding wave. Accordingly, the flow begins to accelerate at the entrance of the bridge openings because of the cross-sectional contraction and the longitudinal profile of the piezometric head drops rapidly along the bridge (Figure 16c). On the contrary, the flow approaching the bridge piers decelerates, giving rise to a local increase in the water level in front of the piers. Moreover, a typical wake develops downward behind the piers (Figure 16a-b), with the outlet of the bridge acting as flow expansion. At the transit of the flood peak, the upstream side of the bridge openings is completely

submerged and the flow under the bridge is mostly pressurized. Finally, the interference between the bridge and the flow produces a noticeable backwater effect over most of the flood event (Figure 16f), and a considerable difference occurs between the water levels upstream and downstream of the bridge at points G1 and G2 (Figure 16e-f), even if the constriction caused by the bridge is relatively short in the flow direction.

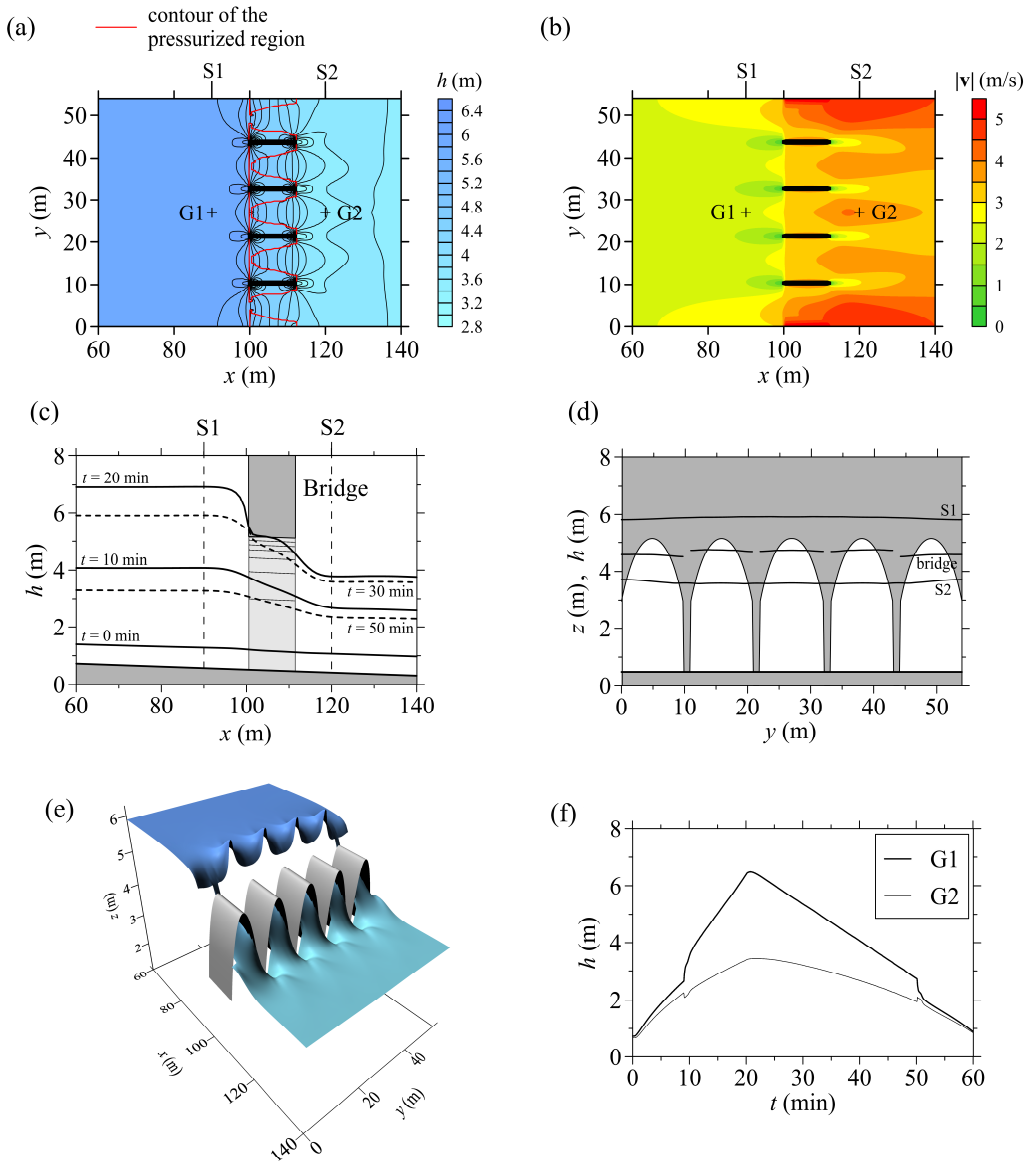

Figure 16. Example of numerical results obtained for the imaginary real-field case study: a) contour map of piezometric head (above a horizontal reference) at t = 30 min; b) contour map of velocity magnitude at t = 30 min; c) longitudinal profiles at different times along the channel centerline; d) cross-sectional piezometric head profiles at t = 30 min for cross-sections S1 and S2 and at the bridge centerline; e) perspective view of the water surface around the bridge at t = 30 min; f) water depth time series at observation points G1 and G2.

5. CONCLUSIONS

The 2D extension of the Preissmann slot model is an effective way of taking into account the presence of crossing structures (such as bridges, culverts, tunnels, etc.), which may flow partly o totally full, in 2D modeling of flood events or flooding processes.

The numerical results show that the proposed treatment of the ceiling discontinuities, which includes the dynamic effect of the structure's deck on the flow in a quasi-conservative finite volume model, provides accurate solutions of theoretical 1D Riemann problems with a top surface step discontinuity and allows the reproduction of significant flow features in the surroundings of a crossing structure potentially running partly or totally full in steady and unsteady laboratory test cases. Therefore, the method can be usefully applied to field scale case studies for hydraulic hazard assessment, even if the local energy loss and the related backwater effect induced by the structure must be expected to be underestimated, especially for high water stages, since the shallow water approximation is inadequate to describe flow phenomena characterized by strong vertical contractions. Nevertheless, the method is simple and robust, and satisfies the *C*-property, i.e. it preserves a static condition exactly, even when the ceiling of the closed structure is partly or totally under pressure.

It is worth noting that, due to the stability condition, computational efficiency may drop dramatically whenever a very fine mesh is used around the structure and especially whenever even few cells under the structure become pressurized. In this last case, very high values of the pressure wave celerity are actually expected. This drawback suggests the adoption of a local time step strategy, already applied to 1D mixed flow modeling by Dazzi et al. [44].

In principle, the limitation of the slot height to the thickness of the structure deck could enable the Preissmann slot approach to deal with the eventuality of the structure being totally submerged by combined overflow and underflow. However, the shallow water assumption may be unsuitable in this case, since the concomitant over- and underflows can form two independent flow layers, especially for long structures. This situation deserves future in-depth analysis due to its practical relevance.

ACKNOWLEDGEMENTS

Prof. J. Murillo is kindly acknowledged for providing the experimental data of the laboratory unsteady test cases. The reviewers are kindly acknowledged for their valuable comments which have greatly contributed to the improvement of the paper.

REFERENCES

1. Bradford SF, Sanders BF. Finite-volume model for shallow water flooding of arbitrary topography. *Journal of Hydraulic Engineering* 2002; **128**(3):289–298.

2. Yoon TH, Kang SK. Finite volume model for two-dimensional shallow water flows on unstructured grids. *Journal of Hydraulic Engineering* 2004; **130**(7):678−688.
3. Aureli F, Maranzoni A, Mignosa P, Ziveri C. 2D numerical modeling for hydraulic hazard assessment: a dam-break case study. In Proceedings of *River Flow 2008*, Çeşme, Izmir, Turkey, 2008.
4. Vacondio R, Aureli F, Ferrari A, Mignosa P, Dal Palù A. Simulation of the January 2014 flood on the Secchia River using a fast and high-resolution 2D parallel shallow-water numerical scheme. *Natural Hazards* 2016; **80**(1):103−125.
5. Mazzoleni M, Bacchi B, Barontini S, Di Baldassarre G, Pilotti M, Ranzi R. Flood hazard mapping in floodplain areas affected by piping breaches in the Po River, Italy. *Journal of Hydrologic Engineering* 2014; **19**(4):717−731.
6. Ernst J, Dewals BJ, Detrembleur S, Archambeau P, Erpicum S, Pirotton M. Micro-scale flood risk analysis based on detailed 2D hydraulic modelling and high resolution geographic data. *Natural Hazards* 2010; **55**(2):181–209.
7. DEFRA. *Afflux at bridges and culverts*. R&D Technical Report W5A-061/TR1. DEFRA & Environment Agency, UK, 2004.
8. Seckin G. A simple formula for estimating backwater at bridge constrictions. *Canadian Journal of Civil Engineering* 2004; **31**(4):561−568.
9. Martín-Vide JP, Prió JM. Backwater of arch bridges under free and submerged conditions. *Journal of Hydraulic Research* 2005; **43**(5):515–521.
10. Picek T, Havlik A, Mattas D, Mares K. Hydraulic calculation of bridges at high water stages. *Journal of Hydraulic Research* 2007; **45**(3):400–406.
11. Aureli F, Dazzi S, Maranzoni A, Mignosa P, Vacondio R. Experimental and numerical evaluation of the force due to the impact of a dam-break wave on a structure. *Advances in Water Resources* 2015, **76**(2):29–42.
12. Malavasi S, Guadagnini A. Hydrodynamic loading on river bridges. *Journal of Hydraulic Engineering* 2003; **129**(11):854–861.
13. Gallegos HA, Schubert JE, Sanders BF. Structural damage prediction in a high-velocity urban dam-break flood: field-scale assessment of predictive skill. *Journal of Engineering Mechanics* 2012; **38**(10):1249–1262.
14. Kara S, Stoesser T, Sturm TW, Mulahasan S. Flow dynamics through a submerged bridge opening with overtopping. *Journal of Hydraulic Research* 2015; **53**(2):186−195.
15. Zhao DH, Shen HW, Tabios III GQ, Lai JS, Tan WY. Finite-volume two-dimensional unsteady-flow model for river basins. *Journal of Hydraulic Engineering* 1994; **120**(7):863−883.
16. Steinebach G, Rademacher S, Rentrop P, Schulz M. Mechanisms of coupling in river flow simulation systems. *Journal of Computational and Applied Mathematics* 2004; **168**(1−2):459−470.

17. Morales-Hernández M, Murillo J, García-Navarro P. The formulation of internal boundary conditions in unsteady 2-D shallow water flows: application to flood regulation. *Water Resources Research* 2013; **49**(1):471−487.
18. Ratia H, Murillo J, García-Navarro P. Numerical modelling of bridges in 2D shallow water flow simulations. *International Journal of Numerical Methods in Fluids* 2014; **75**(4):250–272.
19. Maranzoni A, Dazzi S, Aureli F, Mignosa P. Extension and application of the Preissmann slot model to 2D transient mixed flows. *Advances in Water Resources* 2015; **82**:70–82.
20. Bousso S, Daynou M, Fuamba M. Numerical modeling of mixed flows in storm water systems: critical review of literature. *Journal of Hydraulic Engineering* 2013; **139**(4):385–396.
21. Aureli F, Dazzi S, Maranzoni A, Mignosa P. Validation of single- and two-equation models for transient mixed flows: a laboratory test case. *Journal of Hydraulic Research* 2015; **53**(4):440–451.
22. Kerger F, Archambeau P, Erpicum S, Dewals BJ, Pirotton M. A fast universal solver for 1D continuous and discontinuous steady flows in rivers and pipes. *International Journal for Numerical Methods in Fluids* 2011; **66**(1):38–48.
23. DHI Water & Environment. *MOUSE pipe flow*. DHI Software, Hørsholm, Denmark, 2002.
24. US Army Corps of Engineers. *HEC-RAS. River Analysis System*. Version 4.1. Hydrologic Engineering Centre, Davis, CA, 2010.
25. Cunge JA, Wegner M. Numerical integration of Barré de Saint-Venant's flow equations by means of an implicit scheme of finite differences. *La Houille Blanche* 1964; **1**:33–39.
26. Zhou JG, Causon DM, Ingram DM, Mingham CG. Numerical solutions of the shallow water equations with discontinuous bed topography. *International Journal of Numerical Methods in Fluids* 2002; **38**(8):769–788.
27. Zhou JG, Causon DM, Mingham CG, Ingram DM. The surface gradient method for the treatment of source terms in the shallow water equations. *Journal of Computational Physics* 2001; **168**(1):1–25.
28. Toro EF. *Shock-capturing methods for free-surface shallow flows*. John Wiley & Sons, Chichester, England, 2001.
29. Aureli F, Maranzoni A, Mignosa P, Ziveri C. A weighted surface-depth gradient method for the numerical integration of the 2D shallow water equations with topography. *Advances in Water Resources* 2008; **31**(7):962–974.
30. LeFloch PG, Thanh MD. A Godunov-type method for the shallow water equations with discontinuous topography in the resonant regime. *Journal of Computational Physics* 2011; **230**(20):7631–7660.
31. Greenberg JM, Leroux AY. A well-balanced scheme for the numerical processing of source terms in hyperbolic equations. *SIAM Journal on Numerical Analysis* 1996; **33**(1):1–16.
32. LeVecque RJ. Balancing source terms and flux gradients in high-resolution Godunov methods: the quasi-steady wave-propagation algorithm. *Journal of Computational Physics* 1998; **146**(1):346–365.

33. Chinnayya A, LeRoux AY, Seguin N. A well-balanced numerical scheme for the approximation of the shallow-water equations with topography: the resonance phenomenon. *International Journal on Finite Volumes* 2004; **1**(1):1–33.
34. Bernetti R, Titarev VA, Toro EF. Exact solution of the Riemann problem for the shallow water equations with discontinuous bottom geometry. *Journal of Computational Physics* 2008; **227**(6):3212–3243.
35. Rosatti G, Begnudelli L. The Riemann problem for the one-dimensional, free-surface Shallow Water Equations with a bed step: theoretical analysis and numerical simulations. *Journal of Computational Physics* 2010; **229**(3):760–787.
36. Cozzolino L, Della Morte R, Covelli C, Del Giudice G, Pianese D. Numerical solution of the discontinuous-bottom shallow-water equations with hydrostatic pressure distribution at the step. *Advances in Water Resources* 2011; **34**(11):1413–1426.
37. Yen BC. Open channel flow resistance. *Journal of Hydraulic Engineering* 2002; **128**(1):20–39.
38. Alcrudo F, Benkhaldoun F. Exact solutions to the Riemann problem of the shallow water equations with a bottom step. *Computers & Fluids* 2001; **30**(6):643–671.
39. Wiggert DC. Transient flow in free-surface, pressurized systems. *Journal of the Hydraulics Division* 1972; **98**(1):11–27.
40. Saif A, Hosoda T, Shirai H. Numerical modeling of unsteady flow around a box culvert and its verification. *Journal of Japan Society of Civil Engineers* 2011; **67**(4):I_199–I_204.
41. Van Nam N, Erpicum S, Dewals B, Pirotton M, Archambeau P. Experimental investigations of 2D stationary mixed flows and numerical comparison. In Proceedings of *2nd IAHR Europe Congress*, Munich, Germany, 2012.
42. Toro EF. *Riemann solvers and numerical methods for fluid dynamics*. Springer, Berlin, Germany, 1999.
43. LeVecque RJ. *Finite volume methods for hyperbolic problems*. Cambridge University Press, Cambridge, England, 2002.
44. Dazzi S, Maranzoni A, Mignosa P. Local time stepping applied to mixed flow modelling. *Journal of Hydraulic Research* 2016; **54**(2):145–157.
45. Rosatti G, Fraccarollo L. A well-balanced approach for flows over mobile-bed with high sediment-transport. *Journal of Computational Physics* 2006; **220**(1):312–338.
46. Bermudez A, Vázquez ME. Upwind methods for hyperbolic conservation laws with source terms. *Computers & Fluids* 1994; **23**(8):1049–1071.
47. Vázquez-Cendón ME. Improved treatment of source terms in upwind schemes for shallow water equations in channels with irregular geometry. *Journal of Computational Physics* 1999; **148**(2):497–526.
48. Henderson FM. *Open channel flow*. MacMillan, New York, USA, 1966.

49. Chow VT. *Open-channel hydraulics*. McGraw-Hill, Singapore, 1959.

50. Trajkovic B, Ivetic M, Calomino F, D'Ippolito A. Investigation of transition from free surface to pressurized flow in a circular pipe. *Water Science and Technology* 1999; **39**(9):105–112.

51. Vasconcelos JG, Wright SJ, Roe PL. Numerical oscillations in pipe-filling bore predictions by shock-capturing models. *Journal of Hydraulic Engineering* 2009; **135**(4):296–305.

52. Malekpour A, Karney BW. Spurious numerical oscillations in the Preissmann slot method: origin and suppression. *Journal of Hydraulic Engineering* 2015; 04015060.

List of figure captions

Figure 1. Definition sketch of a 2D computational element with two orthogonal slots added on the top.

Figure 2. Analysis of the effect of a ceiling step discontinuity based on the constant specific force assumption.

Figure 3. Representation of a ceiling step discontinuity in the 2D finite volume discretization by inserting a fictitious cell.

Figure 4. Linear one-sided MUSCL-Hancock extrapolation of intercell variables at a ceiling discontinuity.

Figure 5. a) Wave pattern in the x-t plane of the general solution of the 1D Riemann problem with a ceiling step discontinuity at $x = 0$ (case of a left rarefaction and a right shock). b) Example of solution of the Riemann problem in the u-h phase plane (Test 1 of Table I).

Figure 6. Comparison between analytical solutions and numerical results at different times for the test cases of Table I: a) pressure head; b) velocity ($\Delta x = 0.01$ m, $\Delta y = 0.01$ m, $T_y = \Delta y/10^2$, $T_x = \Delta x/10^6$, $Cr = 0.7$).

Figure 7. Comparison between analytical and numerical unit discharge (a) and total head (b) profiles at a selected time for Test 1 ($\Delta x = 0.01$ m, $\Delta y = 0.01$ m, $T_y = \Delta y/10^2$, $T_x = \Delta x/10^6$, $Cr = 0.7$).

Figure 8. Plan view of the Van Nam et al.'s laboratory set-up [41] for the experimental investigation of steady 2D mixed flows (dimensions in m).

Figure 9. Steady test case by Van Nam et al. [41]: a) contour map of predicted piezometric heads, and b) numerical velocity field for a channel stretch including the culvert.

Figure 10. Steady test case by Van Nam et al. [41]: a) comparison between numerical and experimental piezometric head profiles along the culvert centerline; b) comparison of numerical and experimental x- and y- velocity components at two measuring sections.

Figure 11. Sketch (not to scale) of the laboratory set up of the dam-break experiments by Ratia et al. [18]: a) plan view; b) longitudinal section; c) profiles of the bridge for Tests no. 10 and 8 (dimensions in m).

Figure 12. Example of numerical results obtained at t = 2.5 s around the arch bridge for the laboratory test case by Ratia et al. [18]: a) contour map of piezometric head with reference to the channel bottom, b) contour map of velocity magnitude, c) water depth longitudinal profile along the channel centerline, and d) piezometric head cross-sectional profiles along the bridge axis.

Figure 13. Comparison between experimental and numerical water depth time series for Test 10 by Ratia et al. [18]: a) upstream observation point G_u; b) downstream observation point G_d.

Figure 14. Comparison between experimental and numerical water depth time series for Test 8 by Ratia et al. [18]: a) upstream observation point G_u; b) downstream observation point G_d.

Figure 15. Sketch of the imaginary real-field case study: a) plan view; b) longitudinal section; c) profile of the bridge (dimensions in m).

Figure 16. Example of numerical results obtained for the imaginary real-field case study: a) contour map of piezometric head (above a horizontal reference) at t = 30 min; b) contour map of velocity magnitude at t = 30 min; c) longitudinal profiles at different times along the channel centerline; d) cross-sectional piezometric head profiles at t = 30 min for cross-sections G1 and G2 and at the bridge centerline; e) perspective view of the water surface around the bridge at t = 30 min; f) water depth time series at observation points G1 and G2.

List of table captions

Table I. Test conditions for five Riemann problems with a ceiling step discontinuity.

Table II. Test conditions and numerical results for some selected steady flow experiments concerning a beam bridge (Ratia et al. [18]).

Table III. Test conditions of two selected laboratory dam-break test cases by Ratia et al. [18].